Dissertation for Doctor of Philosophy

Advancements in Medical Image Processing Techniques: From Computerized Diagnosis to Blockchain

Mohamed Yaseen Jabarulla

School of Electrical Engineering and Computer Science

Gwangju Institute of Science and Technology

2020

박사 학 위 논 문

의료 영상 처리 기술의 발전 :

전산화 된 진단에서 블록 체인으로

무하마드 야신 자벨라

전 기 전 자 컴 퓨 터 공 학 부

광 주 과 학 기 술 원

2020

Advancements in Medical Image Processing Techniques:
From Computerized Diagnosis to Blockchain

Advisor: Heung-No Lee

by

Mohamed Yaseen Jabarulla

School of Electrical Engineering and Computer Science

Gwangju Institute of Science and Technology

A thesis submitted to the faculty of the Gwangju Institute of Science and Technology in partial fulfillment of the requirements for the degree of Doctor of Philosophy in the School of Electrical Engineering and Computer Science.

Gwangju, Republic of Korea

May 18,2020

Approved by

Professor Heung-No Lee

Thesis Advisor

Advancements in Medical Image Processing Techniques: From Computerized Diagnosis to Blockchain

Mohamed Yaseen Jabarulla

Accepted in Partial fulfillment of the requirements
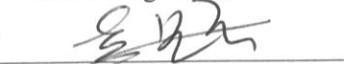
for the degree of Doctor of Philosophy

May 18,2020

Committee Chair _____
Prof. Heung-No Lee

Committee Member _____
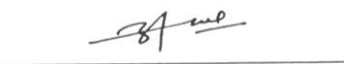Prof. Boreom Lee

Committee Member _____
Prof. Kyoobin Lee

Committee Member _____
Prof. Jonghyun Choi

Committee Member _____
Prof. Anil Kumar (IIITDM, India)

To my grandfather K.M. Mahuduna Rowther,

and my family for their limitless love and support.

Abstract

Healthcare providers and researchers are advancing their image-guided interventions and health management system to provide a flexible, efficient, and early diagnosis for patients. Imaging informatics aims to improve the efficiency, accuracy, usability, and reliability of medical imaging services within the healthcare enterprise. In particular, medical imaging is an essential tool used to create a visual representation of a human body for clinical analysis and medical interventions. Medical imaging includes many types of techniques and operations such as image gaining, analysis, artifact elimination, intelligent noise reduction, secure storage, and communication. Therefore, it is important to focus on research related to medical imaging technologies for routine clinical practice that helps doctors to access and interpret medical images accurately.

This dissertation focuses on solving three distinct issues related to medical imaging techniques: 1) image analysis, 2) image reconstruction, and 3) image management. Our advanced solutions are based on computer-aided diagnosis, computational imaging, and blockchain.

In this thesis, we firstly categorize and review the computer-aided diagnostic (CAD) system according to the five primary stages including data pre-processing, segmentation, feature extraction, feature selection, and classification. The purpose of a CAD system is to process and provide adequate information that helps to analyze ultrasound images for early cancer diagnosis. Secondly, we focus on the image preprocessing stage for reducing multiplicative noise present on

ultrasound image using a sparse representation over a learned dictionary. Thirdly, we proposed a POC design for a distributed framework called a patient-centric image management (PCIM) system. PCIM system is a blockchain-based architecture designed to facilitate secured patient-centric access and storage of encrypted medical images within an open distributed network.

Contents

List of Figures

List of Tables

Abbreviations

B-Mode	Brightness mode
BW-HP	Butterworth high-pass
CAD	Computer aided diagnosis
CT	Computerized tomography
DICOM	Digital imaging and communications in medicine
FFT	Fast Fourier transform
GLP	Gaussian low pass
IPFS	InterPlanatery file system
KSVD	K-singular value decomposition
MRI	Magnetic resonance imaging
OMP	Orthogonal matching pursuit
PACS	Picture archiving and communication system
PCAC-SC	Patient-centric access control protocol using a smart contract
PCIM	Patient-centric image management
POC	Proof-of-concept
SC	Smart Contract
SRAD	Speckle reducing anisotropic diffusion
SR	Sparse representation
TV	Total variation
US	Ultrasound

Chapter 1

Introduction

There are many concepts and approaches for structuring the field of medical imaging [1] that aims to improve the efficiency, accuracy, usability, and reliability of medical imaging services within the healthcare enterprise. Key areas relevant to medical imaging include image processing, image enhancement, computer-aided diagnosis (CAD), and imaging facilities design, etc. Especially, the medical image processing application enables quantitative analysis and visualization of medical images for numerous modalities such as computerized tomography (CT), magnetic resonance imaging (MRI), ultrasound (US) imaging, X-ray and microscopy [2].
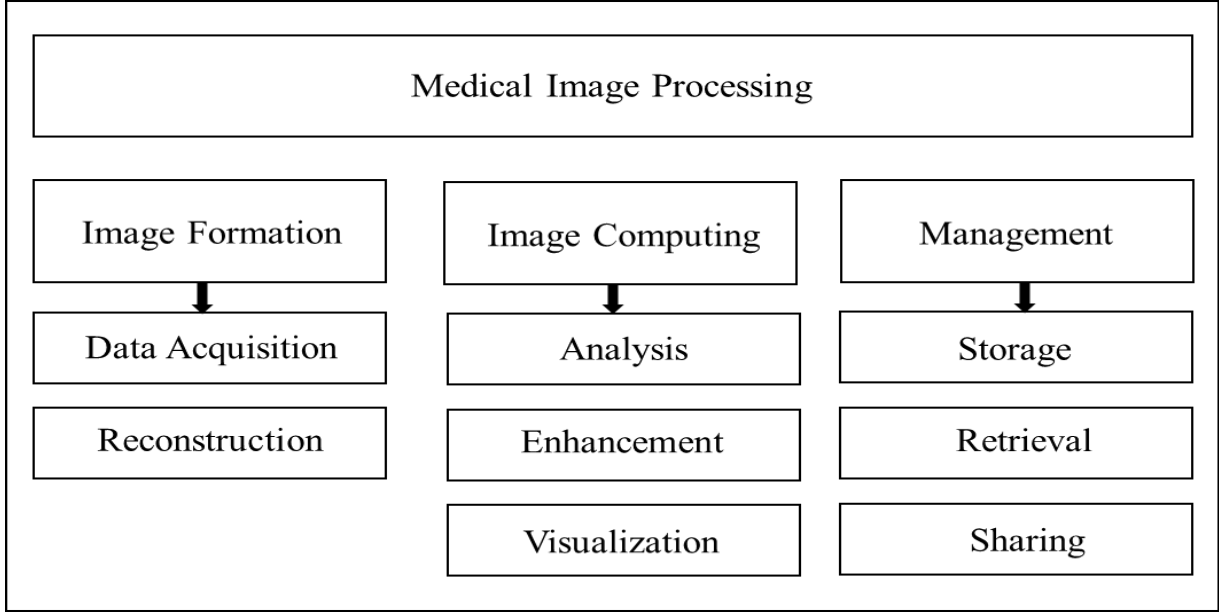
Figure 1: Categorizing the topics in medical image processing

Figure 1 illustrates the core topics of medical image processing. The process of medical image formation is comprised of data acquisition and image reconstruction steps, which provides a

solution to a mathematical inverse problem. The purpose of image computing is to improve interpretability of the reconstructed image and extract clinically relevant information from it. Finally, image management deals with compression, storage, retrieval, and communication of the acquired images and derived information [3]. Overall, medical imaging is a relatively conservative field where the transition from research to clinical applications may often take more than a decade. However, the complex nature of medical imaging embraces multifaceted challenges on all fronts of constituent scientific disciplines, which steadily drives continuous developments of novel approaches. These developments represent major trends that can be identified across the core areas of medical image processing today. Recently, researchers focused on developing revolutionary technologies such as machine learning, artificial intelligence and blockchain for more efficient and effective medical image processing [4]–[6].

In this dissertation, we aim to analyze and reconstruct the US medical images, and we propose a proof-of-concept design for managing medical images in a blockchain framework. Our solutions are based on the potential of three core technologies: Computer-aided diagnosis, computational imaging and blockchain. In the following subsections, we briefly discuss these core technologies, and we present contributions of this work to overcome the problems in medical image processing.

1.1 Image analysis using computer-aided diagnosis

In chapter 2 we provide an in-depth overview of analyzing US liver images using CAD system for early diagnosis. CAD is an approach that has the potential to improve traditional histopathology image analysis. CAD system can be applied to numerous medical imaging modalities such as CT, MRI, US imaging, and nuclear medicine[4], [7]–[9]. CAD system includes multiple concepts like artificial intelligence, computer vision, and medical image processing [10], [11]. The main goal of

chapter 2 is to investigate various components and algorithms of CAD system. The investigations of CAD system used to identify abnormal lesions on a human body and to improve the capability of radiologists by analyzing the US images. US is an easily available inexpensive imaging tool, without accompanying the risk of radiation. However, analyzing US images manually is not an easy task. Therefore, to support the diagnosis of clinicians and reduce the work load on doctors, many US computerized systems are proposed for preoperative staging [10], [11], follow-up after cancer treatment, and interventional diagnosis.

1.2 Image reconstruction using computational imaging

The goal of computational imaging is to extract additional information through advanced image processing algorithms. Using principles of computational imaging, one can design an instrument to make measurements from which images, and other scene information, can be derived with a capacity that far exceeds the physical limits of the signal processing [12]. Computational Imaging systems cover a broad range of applications such as computational microscopy, CT, MRI, US imaging, computational photography, synthetic aperture radar (SAR), etc [13]. In chapter 3, we proposed a speckle reduction algorithm for US liver images based on sparse representation. The goal is to remove speckle noise while preserving the texture and yielding a smoother image than conventional approaches.

1.3 Image management using blockchain

Medical image sharing is the electronic exchange of medical images between hospitals, physicians and patients. Medical images are typically shared on CDs or DVDs shipped between hospitals, physicians, and patients during the course of clinical diagnosis and treatment. However,

applying these technologies might lead to damage or interception of medical images resulting from patient or physician errors [14]. To overcome the shortcomings of physical media transfer, a cloud-based technology was introduced to share, archive, and store medical images across various healthcare enterprises, usually in a format called digital imaging and communications in medicine (DICOM) [15], [16]. Recently, several researchers focused on developing a framework that combine a cloud service and a blockchain [17], [18] for the purpose of secure medical health record sharing. In chapter 4, we provided a brief overview on the structure of the proposed patient-centric image management (PCIM) system and illustrated interactions among different components of the system using the access control protocol.

1.4 Original contribution

There are several original contributions made in this thesis:

➢ A systematic review on computer aided diagnostic system for early detection of liver cancer.

➢ A multiplicative speckle suppression technique for US liver images has been proposed.

➢ A patient-centric access control protocol using a smart contract (PCAC-SC) for a medical image exchange has been proposed.

1.4.1 Thesis outline

This thesis is organized as follows: the medical image processing and its areas are introduced in Chapter 1. In Chapter 2, we present a brief overview of computer aided diagnostic system for US cancer images, which were published in [19]. We outline a number of challenges and highlights opportunities for further development.

[19] Mohamed Yaseen.J, Heung-No Lee, "Computer Aided Diagnostic System for Ultrasound Liver Images: A Systematic Review", *Optik - International Journal for Light and Electron Optics Optik.*, vol. 140, pp. 1114–1126, July 2017.

In Chapter 3, we evaluate and propose a speckle reduction algorithm based on sparse representation, some part of which were published in [20] and [21].

[20] Mohamed Yaseen.J, Heung-No Lee, "Speckle Reduction on Ultrasound Liver Images Based on Sparse Representation Over Learned Dictionary" *Applied Sciences-MDPI.* Vol. 8, no, 6, pp 903, May. 2018.

[21] Mohamed Yaseen.J, Heung-No Lee," Evaluating the Effect of Various Speckle Reduction Filters on Ultrasound Liver Cancer Images". ICEIC 2018, Hawaii, USA.

In chapter 4, we design a proof of concept for a distributed framework called a patient-centric image management (PCIM) system [22]. This is a blockchain based architecture designed to facilitate secure patient-centric access and storage of encrypted medical images within an open distributed network, and in chapter 5, we conclude the thesis.

[22] Mohamed Yaseen.J, Heung-No Lee, "Blockchain-Based Distributed Patient-Centric Image Management System", preprint arXiv:2003.08054, March *2020.*

Chapter 2

Computer aided diagnostic system for ultrasound liver images: A systematic review

In this chapter, we provide an in-depth overview on computer aided diagnostic (CAD) systems for liver cancer. Besides, in a broader sense highlighting the technical aspects developed for medical ultrasound images is also discussed. CAD system is a process that provides adequate information that helps to analyze the ultrasound images and helps to accurately detecting different types of liver cancer. However, the system performance is still not significantly improved.

In this chapter, firstly, we categorize the CAD system according to the four primary stages including data preprocessing, lesion segmentation, feature extraction, selection, and classification. In each stage, we review specific methods that are commonly used in most of the algorithms proposed for computerized tissue characterization and discuss their advantages and drawbacks. Then, recently proposed algorithms are presented in summarize form that have shown clinical value or specific possibility to the computerized analysis of setback for ultrasound liver images. These techniques or their combinations are the ones that are mostly used in the past few decades by the majority of work published in the computer aided diagnosis domain.

2.1 Background and contributions of this work

Sonography is a widespread medical imaging method whose principle is based on the propagation of ultrasonic waves in biological tissues. It allows real-time visualization of body

structures by displaying their acoustic properties. Ultrasonography has the advantage of being non-invasive, non-ionizing, and relatively cheap compared to other imaging methods such as X ray imaging. In practice, a probe emits an ultrasonic wave, which is then diffused, reflected and attenuated by different tissue structures. Part of the wave travels back in the direction of the probe, which performs its acquisition and conversion to an electrical signal.

For US liver image diagnosis CAD strongly depend by the quality of data. The comparatively substandard of clinical US images reduces the success of early liver ailment finding and analysis. The data generated by the automated computer processes while diagnosis is helpful to the radiologist to realize the US liver images. So, the precision of image diagnosis is better, and the time required by regular methods in peruse an image is reduced [23]. Henceforth, utilizing CAD the analysis of diseases has become a vibrant area of research [24]. There is greater requirement of precisely analyzing the therapeutic images and lessening the time requisite for proper analysis of liver cancer.

The key objective of this review is emphasizing on the potentiality of intelligent computer systems to be utilized in clinical application to support pathologists to analyze and classify US liver cancerous tissue images. On the basis of methodical analysis of various liver conditions, CAD methods and organized summary of algorithm, we categorize the computerized system according to the four primary stages of analyzing liver US image. Here the using of general procedures including data preprocessing, lesion segmentation, feature extraction and selection, and depicting of cancer by means of a classifier [25] better summarizing the performance of each category leads to find the ideal solution for automatic computerized system performance and the four stages are given in Figure 2.

➢ Data preprocessing: The preprocessing task is to restrain the noise and to increase the image without eliminating the important features of liver US images.

➢ Image segmentation: Here image is divided into a number of small portions, and it forms the background the lesions detached. The edges of the lesions are outlined for feature withdrawal.

➢ Feature extraction and selection: The stage identifies a feature set of liver cancer lesions that can precisely differentiate normal tissue or abnormal cancer tissue. The feature space could be vast and intricate, so withdrawal and choosing the finest features is decisive.

➢ Classification: After the selected features, the apprehensive regions will be characterized into distinctive classifications, say normal tissue or cancerous tissue.
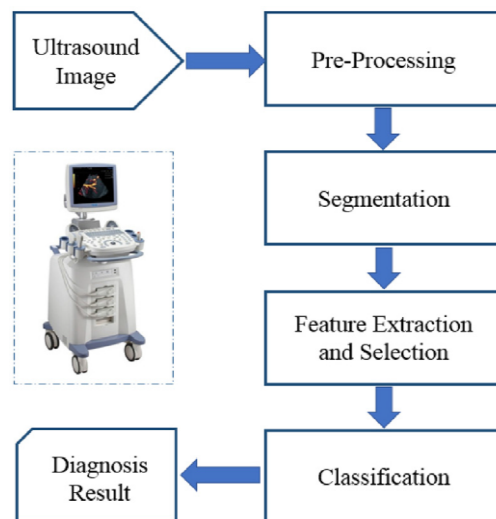
Figure 2: Flow diagram of CAD for liver cancer.

2.2 Classification of liver cancer

Globally liver cancer is much popular malignant disease, mainly in Southeast Asia and sub Saharan Africa. Worldwide, liver cancer has sixth position as the most familiar cancer with a half

a million people affected each year. The number of people who develop liver cancer is increasing around the globe [26].

In human body liver is one of the indispensable organs. It's extremely hard to live without a sound liver because of its impacts on every other body parts. Mainly focal liver diseases and diffused liver diseases influence the liver. Diffused liver diseases, for example cirrhotic and fatty, harm the total surface of liver. Focal liver diseases which affect the small area of the liver surface, such as hepatocellular carcinoma (HCC), hemangioma (Hem), and cyst. Fig. 3 presents three focal liver diseases in the US images. The hepatocellular carcinoma (HCC) and echo type in the liver based on US image representation, five types of primary carcinoma of liver tumor are there, they are correlative to low echo type, equal echo type, high echo type, mixed echo type and diffuse type correspondingly.

Complexity of the liver tumor in patients having chronic viral illnesses, can be classified from asymptomatic strong carriers to patients with liver cirrhosis [27], [28]. In general, the US appearance of Cyst, Hem, and HCC visible similar. Brightness mode (B-mode) ultrasound [29] diagnosis is the foremost choice in well-liked analyses because of its effectiveness, non-invasiveness, and economy. All types of liver cancers are not correctly diagnosable in the US images, in case there is benign appearance of deadly tumors and observer's diagnostic level is not good, careless mistakes and visual fatigue. Hence, utilizing traditional method it is extremely difficult in decision making between them. A fully efficient automatic computer system is required to be developed for disease detection and diagnose with high performance.
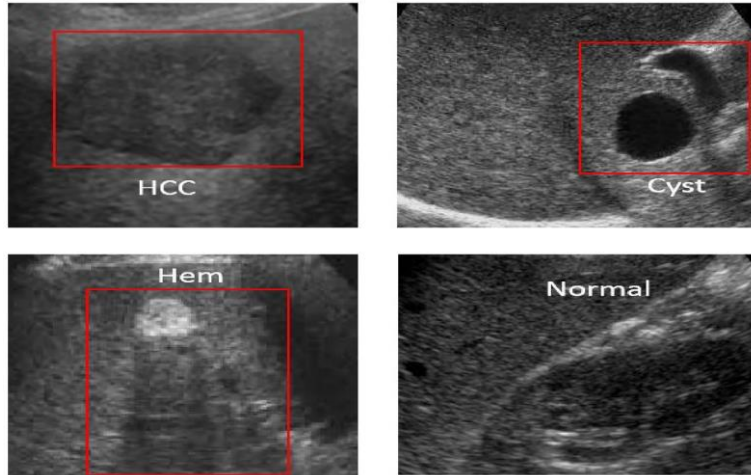
Figure 3: Normal liver and focal liver US images.

2.3 Overview of the CAD system schemes

The most recent success in automatic diagnosing of liver US images is reviewed in this section. The four main steps in the CAD including data preprocessing, lesion segmentation, feature extraction and selection, and classifier of lesions are discussed in detail.

2.3.1 Data preprocessing

Data preprocessing is aimed at filtering speckle noise, which impinge on the diagnostic value of the US image [30]. It makes image detail unclear and hazy drastically, demeans the image feature. Likewise, it decreased the pace and correctness of US image processing tasks say- division and classification. Hence, in US image processing tasks, speckle noise reduction is always an important prior requirement. Fig. 4 depicts an example for speckle noise image and enhanced image.

In this chapter, we categorized the speckle reduction techniques into two major classifications, namely a) spatial filtering methods and b) multiscale methods. Those methods are effective in eliminating the speckle noise and conserving the analytical information in US images.
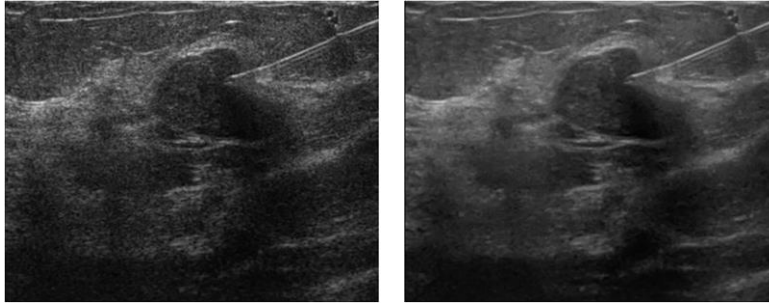
Figure 4: (Left) Speckle noise image and (Right) Despeckled US image.

Spatial filtering process

The basis of spatial filter is proportion of local statistics. It is helpful to improve smoothing in uniform regions of the US images where speckle is completely visible. This method lessens smoothing substantially in surrounding areas of the image to conserve the helpful particulars of the image [31]. Lee and Kuan Spatial filters use local statistics to perform straight on the intensity of the image [32]–[34].

Various sorts of filters are utilized as a part of uses of speckle lessening in US imaging. The most usually utilized sorts of filters are:

- Mean filter [35] is easy to apply, also its a plain filter . However, speckles are not eliminated by it, but in the data averaged by it. It is an attractive technique for speckle noise diminishing as it can make loss of resolution and accuracy Image can be obscured by it. It has amazing quality for added substance Gaussian noise, though the speckled image comply a multiplicative form with non-Gaussian noise since the mean filter is not an ideal selection.

- Median filter [36] is very efficient against impulsive type noise and edge conserving characteristics. It generates least obscure images in comparison to mean filter. It requires listing of all near values into numerical order to figure out the median and here it is the

drawback. Moreover, it takes additional calculation time to list the intensity value of all set.

- Wiener filter [37], [38] replace images in the existence of noise and blur. Decreasing the quantity of noise presence in a signal by comparing with an assessment of the preferred noiseless signal is the aim of algorithm here. The approach of filter towards image smoothing is on the basis of calculation of local image variation. The smoothing becomes less when the local variation of the image is immense. The filter does more smoothing when the difference is small. This calculation over linear filtering over linear filtering. It conserves edges and other high recurrence information of the images, however takes more time for calculation than linear filtering.

- Enhanced Frost and Lee filter [39] is utilized to vary the capability in light of the limit value. The filter works out like a stern all pass filter when the local coefficient of variation is over a greater limit. On the other part as the local coefficient of variation goes under a poor limit then pure averaging is actuated. The stability amongst averaging and identity operation is processed when the coefficient of variation stands at middle of lower and higher thresholds.

- Gamma Map filter [40] is like preceding filter aside from that the local coefficient of variation takes place amid the two limits; the filtered pixel value depends on the Gamma estimation of the contrast proportions inside the proper filter window. It is utilized to reduce the loss of texture information. The filter needs suppositions about the dispersion of the genuine procedure and the degradation model.

- Frost filter [41] is an adaptive and exponentially weighted average making filter in light of the proportion of the local standard deviation to the local mean of the debase image. Within

the $n \times n$ moving core it interchanges the region of interest with a weighted sum of the values. The weighting aspects lessen with difference from the region of interest. The weighting aspects increment in the mid region as difference inside the core grows.

- Lee filter [32], [33] relies upon the multiplicative speckle model. It can utilize local statistics to conserve borders and attributes adequately. It also uses the process like when the variance over an area is poor, then the smoothing will be done. When the difference is much similar to near borders, no smoothing will be done.

- Kaun filter [42] Relies upon an image's Equivalent Number of Looks (ENL) to decide an unlike weighting function to do the noise reduction. The filter model is a local linear least square inaccurate filter relies on multiplicative model regarded as to be finer to Lee filter. It makes no estimation of the noise variance inside the filter window.

- Diffusion filter is for smoothing images on a nonstop area, nonlinear partial differential equation was implemented by Perona and Malik [43], which has since been extended and enhanced [44], [45]. Through many years, other denoising processes with extremely fascinating ability are developed for example: Bilateral filter along with derivatives [46]. In Speckle reducing anisotropic diffusion (SRAD) [47] dispersion of speckled images is edge-sensitive. Its preference is a rapid and a decent speckle lessening impact. In SRAD, the instantaneous coefficient of variation goes about as the border identifier. Here algorithm displays maximum gains at the borders and creates least gains in consistent areas. This way, it guarantees the mean-preserving conduct in the uniform areas, and conserves and improve the borders. The noted diffusion methods can save or even improve important edges when taking out speckles. Even so, the techniques have one basic constraint in holding unobtrusive features of minute cyst and lesion in US images.

Multiscale process

For US imaging numerous speckle reduction algorithms are proposed in light of contourlet, curvelet and wavelet.

- Wavelet Transform: The key target of speckle diminishment is eliminating the speckle noise by not missing much data included in an image. To be successful this target Wavelet transform have set up since it gives an ideal representation for 1D (single dimensional) piecewise smooth signals, for example, an image's scan lines [48].The complex wavelet transform (CWT) just requires $O(N)$ computational to enhance directional selectivity. Yet, in the past intricate wavelet change not broadly utilized, as it is hard to devise intricate wavelets with impeccable recreation properties and good filter attributes [49], [50]. Kingsbury proposed the technique known as dual-tree CWT in articles [51], [52], which can add faultless reform to the other appealing properties of difficult wavelets, incorporating limited redundancy, estimated shift invariance, six directional selectivity's, and proficient $O(N)$ calculation. To build 2D complicated wavelets here Tensor-product 1D wavelets are utilized. The directional discerning dispensed by complicated wavelets (six directions) is vastly improved from what is acquired by the discrete wavelet transform (three directions), however is by now fewer. Such undesirable practices demonstrate that further potent representations are asked in upper dimensions.

- Contourlet Transform: A contourlet transform utilizing 2D transform process for image delineation and study executed by Do and Vetterli [53]. It was implemented in the detached space. likewise, the researchers justify its union in the uninterrupted space. It was implemented in a detached space multiple direction and a multiple resolution extension utilizing non-distinguishable filter banks. This brought about an adaptable multi-resolution, directional and

local image extension using contour segmented region, and hence it is known as contourlet transform. As specified before by utilizing a filter bank that decouples the multiscale decomposition contourlet was completed and finished by Laplacian pyramid and then directional decompositions, which are completed utilizing a directional filter bank. The advantages of contourlet alter are as follows. 1) The rectangular grids are utilized to portray contourlet expansions, and thus offer an impeccable interpretation to the distinct world, where based on a rectangular grid the image pixel's sample is taken. The main disparity between the contourlet [53] and the curvelet framework [54] are to attain the rectangular grid attribute, the contourlet kernel roles have to be diverse courses and by just turning a lone function cannot be acquired. 2) As a consequence of rectangular grids, contourlet have 2D division on centric squares, besides centric circles for curvelets and polar coordinates to depict other systems. 3) Since usage of iterated filter banks for wavelets, contourlet transform utilizes quick bank calculations and adaptable tree structures. 4) This calculation gives a space multi-resolution action plan which gives lithe improvements of the spatial and angular resolution. The contourlet change characterizes a multiple scale and multiple directional delineation of an image. Likewise it is simply adaptable for identifying superior attributes in any placement at a variety of scale levels [55] ensuing in fine probable for efficient image examination.

- Curvelet Transform: A new algorithm is presented by Candes and Donoho in article [54] on the continuous 2D (two-dimensional) space R^2 utilizing curvelets. This calculation showed a fundamentally ideal estimation manner for 2D per piece plane functions that are curves. First generation curvelet transforms are deliniated in the uninterrupted domain [54] through multiscale filtering and after that on each bandpass image applied a block ridgelet transform [56]. The second generation curvelet transform [57] was produced utilizing no ridgelet

transform but using frequency partitioning. However, for implementing both curvelet generation want a turning maneuver and ought to match with a 2D frequency division on the basis of on the polar coordinate. It gives the curvelet creation easily in the uninterrupted sphere, yet makes it critical sampling appears to be troublesome in discretized structures. The curvelet change is extremely proficient in representing curve-like edges. In any case, this transforms have two key disadvantages: 1) the discrete curvelet transform is superfluous. 2) They are not ideal beyond c^2 singularities for sparse approximation of curve features. On US images most standard speckle filters perform fine, yet a few limits exist with them, which lead to image resolution degradation. In this way, while developing an efficient and strong denoising algorithm for data preprocessing stage in CAD one needs to consider various factors. In the design of despeckling methods, choices of despeckling filter and speckle model have important part. In above most usually favored models and filters were reviewed with its pros and cons.

2.3.2 Segmentation

Segmentation process is a mandatory step in CAD systems that frequently refers to the delineation of specific structures [58]. Segmentation's key objective is to convert the image to provide more significant data that can be effortlessly examined. It is used to distinguish the various boundaries and objects in images. Due to poor contrasts, different types of noise and missing the boundaries in medical images make segmentation Harder. Depending on anyone between the two vital traits of intensity values that are similarity and discontinuity Medical image Segmentation approaches are mostly based [59]. In subsection, the different segmentation procedures of the medical images are reviewed and it is composed into four basic classifications as appeared in figure 5.

Region based method: On the basis of pixel alikeness in a region, these process is developed. It is used to approximate the region straight [60], [61]. This method classifies the pixels with comparable attributes (like intensity) into regions. Classification of Region based methods have two methodologies such as- a) region expanding approach and b) region combining/dividing approach. In this approach, the procedure initiated by choosing a seed region (pixel). Adams and Bischof [62] proposed the first seeded region growing. The region develops by including the neighbor pixels having comparative established in advance standard with the seed, for example-texture, potency, difference, texture or gray level, etc. When no pixel is present for inclusion then the procedure stops. The issues with this approach are- the user has to choose the seed point and it will miss the efficacy when the region is inhomogeneous. Within the region, combining/splitting mode, the technique starts with the entire image as a seed. At that point, the seed is partitioned into various sub regions, most often into four sub regions. Thus, continuity of the process goes on till there are no regions of the partition by using each sub region as a seed. Lastly, based on same properties, for example intensity, variance or gray-level combine any adjacent regions.
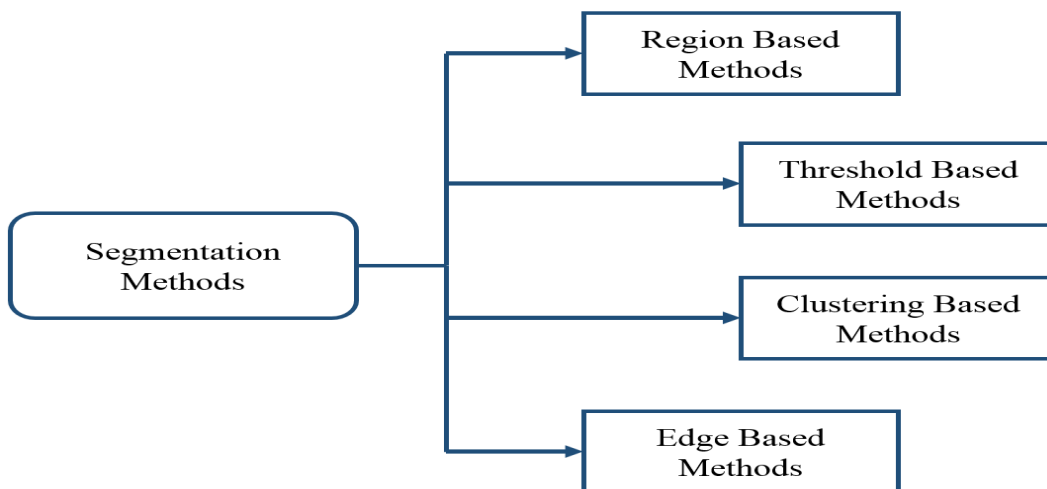
Fig. 5. Image segmentation methods.

Edge based methods: Edge based methodology [60], [63] utilized for distinguishing the discontinuities in an intensity value for image segmentation. It is the sudden changes in potency

level at the region borders of US images. The image border can be described as the perimeter isolated by different areas that vary in the level of potency [64]. Utilization of the borders are to identify the items' measurement and differentiate items from the background. Usage of edge detectors are needed to trace the distinctive points in the image where the potency actually changes. Border detection is a vital tool for the success of segmentation and interpreting the US image content, mainly when dealing with feature extraction and feature detection. There are two main techniques in order to detect an edge in US images such as searching and zero crossing techniques. Figuring the gradient magnitude by making use of first order derivative expressions takes place at first place in search-based technique. Subsequently, with the utilization of gradient direction local directional maxima of the gradient enormity is searched. In zero crossing technique, looking for a zero crossings in the second imitative of the image takes place. Finding zeros in the second imitative of image orders are detected, at this time the value of first imitative is high and zero is the value of second imitative. It is named Laplacian approach on the basis of edge detection. The edge based division method's disadvantage is, when there is presence of lots of edges in the image it does not work well.

Threshold based methods: For image segmentation, Thresholding [65] is one of the imperative techniques used. It is helpful in a separate frontal region from the background region of the image. The gray level image can be changed to binary image by choosing a sufficient limit value T, All necessary data regarding the shape and position of the objects of interest (foreground) and the image's (background) other areas ought to be contained in the binary image. To acquire data easily gray image conversation to binary image is done, that result in the generalization of the categorization phase. Pixels having unique concentration less than the threshold rate is named "black pixels" (0) and belongs to the background. On the other hand, pixels over the threshold rate

is called "white pixels" (1) and becomes object's part. There are two sorts of thresholding systems: a) global thresholding and b) local thresholding. There is fixed value of threshold T in global thresholding. Such threshold's difficulty is, if the background of the image holds unlike enlightenment, failure of segmentation procedure may occur. In local limiting, the threshold value T is not fixed, as such the problem of particular enlightenment can be sorted out by using numerous thresholds. Automatic threshold scheme utilizing different routines for example Mean, Edge maximization technique (EMT), Histogram dependent technique (HDT) is a system where [60] threshold value T for every image is automatically selected by the system exclusive of human intrusion.

The histogram-based techniques are dependent on achieving the estimated threshold value T. This threshold value T divides the two uniform backgrounds and area of the item in the image. The image having a uniform area of the item and background and separated by heterogeneous region between them, the HDT is appropriate for it. In mean based framework, the threshold value T utilizes pixel's mean value and work fine in stringent cases of the images that have generally partly of the pixels connected with the objects and the rest half associated with the background.

The EMT segmentation system relies on finding the most border limit in the image to begin segmenting with the guide of border recognition process works. It is applied when the image holds excess of one uniform area or where there is an alteration in lighting between its background and item. As it occurs, the object sections may be united with the backdrop or a portion of the backdrop may be united with the item.

The inconvenience of thresholding method is barely two categories are created, and it cannot be tried on multichannel pictures. Thresholding does not judge the spatial distinctiveness of an image so it is irritable to noise. This distorts the histogram of the image, making the separation more

troublesome. In general, thresholding procedures are reasonable for images that hold more and clear separation between the homogenous regions. It has resulted to enhance the effectiveness of the threshold technique.

Clustering based method: It is an unattended learning undertaking, where it perceives a limited set of classes known as clusters to categorize pixels [66]. Clustering performs by either grouping pixels or partitioning pixels. In the grouping type, it starts with every component as a distinct bunch and combines all the distinct clusters in forming bigger clusters. While, in partitioning type, it begins to split into successively smaller clusters from the entire image.

The clustering techniques are divided to attended clustering and unattended clustering. In attended clustering to decide the clustering properties, Human interactions required. Whereas in unsupervised clustering technique, by own help the clustering properties are defined. There are two popular algorithms for unsupervised clustering that are, K-mean clustering and fuzzy clustering.

1) K-mean clustering: It is an unattended clustering calculation. It categorizes the input data points into numerous categories based on natural space from one another. Here data vectors are organized into predefined number of clusters. At first, the centroids of the predefined clusters are initialized arbitrarily. The centroid and data vector dimensions are same. Every pixel is consigned to the cluster on the basis of nearness, estimated by the Euclidian distance measure. Following every one of the pixels are clustered, the average of every cluster is recalculated. Repetition of this procedure goes on until no noteworthy vary outcome for some fixed number of iterations or for each cluster mean [67].

2) Fuzzy clustering/Fuzzy c-means (FCM): it is an unsupervised clustering algorithm. Here a dataset is grouped into n clusters with all data point in the dataset staying with all bunches to an

exact degree [68]. The Fuzzy clustering technique can be thought to be better than those of their harder counterparts, since they can represent the affiliation between the input pattern data and clusters more actually. Fuzzy c-means is a most prominent soft clustering technique; its viability to a great extent is limited spherical clusters. It has extra advantage as it is extra lithe than the corresponding stiff clustering algorithm.

2.3.3 Feature extraction and selection

In the detection and classification of liver cancer feature drawing out and choice [69] are significant course of action. However, in computer-aided system only texture features are used as inputs. Texture feature extraction is the basic and traditional techniques. Different examination techniques are used to extract helpful attributes for US liver cancer image classifications. A few general utilization systems are:

Laws Texture Energy Measure (TEM): In order to find various texture types of TEM [70] using convolution masks of 5x5. It works to produce 25 2D masks by convolving based on 5 basic 1D masks. Afterwards texture picture is filtered with produced masks by extracting helpful attributes.

Gray Level Difference Statistics (GLDS): It is the Probability Density Function of pair pixels lying at a particular difference and holding a discrete potency value variation. Least variation of coarse texture and large variation of fine texture in Inter pixel gray level values.

Spatial Gray level Dependence Matrices (SGLDM) [71]: It counts how often pixels with a potency i and j happen at a particular offset to calculate matrix. It makes use of spatial relationships amid gray levels of a picture furnishes to total texture properties of the picture

Gray level Run length Statistics (GLRLM) [72]: Its rough texture consists of comparatively long runs than short runs. It utilizes fact that containing similar gray level along a particular course of the successive points in the image.

Gray Level Histogram: Texture parameters are obtained by using the intensity distribution of the image.

Fourier Power Spectrum (FPS): FPS used for normal wave like forms with a fixed interval. Fourier conversion gives the frequency of form and direction.

Edge Frequency on the basis of Texture Features: It is opposite to the autocorrelation role and depending on difference concerned gradient little and big distance operator is detected using Micro-edges and macro-edges.

Wavelet Features: It is derived from Region of Interest (ROI) or wavelet transform of the image. Foremost types are quincunx, Gabor and dyadic.

First Order Parameters (FOP): It defines only diffuse variation and echogenicity characteristics and these are sovereign of spatial concern amid pixels.

Successive texture analysis methods depend on selecting appropriate features. Some important textural features include- contrast (CO), Short Run Emphasis (SRE), Local Homogeneity (LH), Energy (E), Gray Level Distribution (GLD), Variance (VAR), Homogeneity (H), Uniformity (U), Sum Entropy (SENT), Dissimilarity (D), Angular Second Moment (ASM), Run Length Distribution (RLD), Mean (M), Inverse Difference Moment (IDM) and Standard Deviation (SD).

2.3.4 Classification

After extraction of feature and selection process, we have to classify the images into lesion/non-lesion or normal/abnormal classes. Classifiers are divided into two types - statistical and neural network, which can be classified using unattended as well as attended procedure. An example for numerical unattained classifiers such as K means clustering [73] and for statistical attained classifier e.g. Support Vector Machine (SVM) [74], [75]. In the meantime for unattended neural grid like Self Organizing Map (SOM) [76] and for attended neural grid such as Multi-Layer Perceptron (MLP) [77], [78] are utilized to classify liver images. We summarize the different US liver detection and classification techniques are listed below

Fuzzy neural network (FNN): Diverse stochastic associations are find out by it, which represent the attributes of a picture. The diverse sorts of stochastic are grouped (set of attributes) in which the elements of this set of attributes are blurry. It gives the scope to define various classes of stochastic attributes in the comparable type [79]. Accomplishment and correctness depend on the limit choice and unclear integral. The drawback of fuzzy neural network is exclusive of previous information output is not fine and accurate result depends on the route of decision.

Support vector machine (SVM): SVM targets to reduce the superior bound of generalization fault by increasing the periphery amid the parting hyperplane and the data [80]. Fine division is gained by the hyper plane that has the biggest difference to the closest training data point of any class (operating margin), usually bigger the margin lowers the generalization mistake of the categorizer. SVM utilized Nonparametric with binary classifier approach. It can manage additional input data extremely proficiently. Accomplishment and accurateness depend on the hyperplane choice and core limit. SVM reduces the calculating difficulty, easy to administer decision rule intricacy and fault occurrence. The drawbacks of SVM are low result transparency, training is time consuming

and finding out of finest limits is not trouble-free in presence of nonlinearly separable training data.

Artificial neural network (ANN): It is the combination of arithmetic techniques inspired by the characteristics of biological nervous system and the tasks of versatile biological learning models. Its plain formations are neurons that can be interrelated in distinctive arrangements. It utilizes a nonparametric method. Accomplishment and accuracy depends on the grid formation and the quantity of inputs. There are many types of ANN classifier, but only few algorithm proven efficiency in neural network learning like multi-layer back propagation [81], [82]. The advantages of ANN are a data driven self-adaptive process, competently controls noisy inputs, calculation rate is good and its major problem is taking more time for training data and complexity in selecting the type grid architecture.

Probabilistic neural network (PNN): There are input, output and hidden (summation) layer in Feed Forward Neural Network. Pattern layer formed by the input data set with the product of the weights tracked by the summing up layer that gets results related to the given class. The output layer contains the classification results. The main advantage of PNN classifier is its maximum training speed [83]. The scale factor of the exponential activation functions used to control the smoothing parameter (σ) of this classifier.

Decision tree: In medical image study it is used as a attended categorizer. This process is comprised of 3 parts- Dividing the nodes, locate the terminal nodes and sharing of class labels to terminal nodes. A node in a tree represents a test for a exact attribute, and each part of that node represents the likely result of the test [84]. A pathway in the tree, from the root of the tree to an end leaf, details the categorization, with the ending leaf representing an object class. The Decision tree is based on the hierarchical statute based method and utilizes the nonparametric process. It is simple

and computational efficiency is good, but becomes a difficult computation when diverse values are undecided or when variety of results are correlated.

K-nearest neighbor (K-NN): It is a process to analyze image feature on basis of closest training illustrations in the feature space. It utilizes a separate calculate to make guess the class of the new test sample. This technique is one of the least complex of all machine learning calculation: a feature is arranged by a maximum vote of its neighbors, with the item being allocated to the class most ordinary amongst its k adjacent neighbors when k is small and the item is merely assigned to the class of its adjacent neighbor when K=1 [85].

Bayesian neural network (BNN): It used in many areas of medicine. In US features prophetic of malignancy have been widely analyzed and the reactivity and specificity of these attributes for malignancy are easily obtainable [86]. The scheme of BNN is to cast the work of training a grid as a difficult of inference, which is sorted out utilizing Bayes theory [87]. A Bayesian neural network is extra optimized and strong in comparison to traditional neural grids, particularly when the training data set is not big.

2.4 Performance estimation

Quantitative measurement of system correctness is measured in term of true positive (TP), true negative (TN), false positive (FP), false negative (FN) with relation to positive predictive value (PPV), negative predictive value (NPV), sensitivity, specificity and accurateness [88]. It is given by:

$$PPV = \frac{(TP)}{(TP + FP)}$$

$$NPV = \frac{(TN)}{(TN + FN)}$$

$$Sensitivity = \frac{(TP)}{(TP + FN)}$$

$$Specificity = \frac{(TN)}{(TN + FP)}$$

$$Accuracy = \frac{(TP + TN)}{(TP + FN) + FP + FN}$$

- *TP* represents number of diseased lesions that is rightly classify as diseased.

- *TN* represents number of non-diseased lesions that is properly classify as non-diseased.

- *FP* represents number of non-diseased lesions that is incorrectly categorized as diseased.

- *FN* represents number of diseased lesions that is incorrectly categorized as non-diseased.

- The accuracy used to diagnose diseased and benign cases, the sensitivity calculated for the classification model to categorize diseased cases and the specificity used to evaluate benign cases.

- *PPV* represents percentage of predictive positives that is always positive.

- *NPV* represents percentage of predictive negatives that is always negative.

Some authors have evaluated their proposed system just by manual inspection performed by radiologist Specialists while others have exploited area under receiver operating characteristic (ROC) curve analysis. ROC applied to demonstrate the competence of the trade-off between the *TP* and the *FP* [89].

2.5 Related Work

In recent years, the liver cancer analysis using CAD system has turned into a dynamic area of research. There are different approaches that are proposed for liver ailment analysis on the basis of medical picture analysis. In this section, we elaborate various techniques.

In article [78], a CAD system is proposed by Mittal et al. by which doctors can be guided in diagnosis of focal liver ailment from 2D mode US images. The suggested technique has been utilized for detecting and analysis of four types of focal liver ailment and compared them with normal liver. At the first image noise are reduced, then they divided the areas of interest to 800 segmented areas. Next, on the basis of the texture 208 features are extracted from each segmented region. Finally, they proposed use of Artificial Neural Networks (ANN) in reducing the training errors with two phases to diagnose the ailment. The general precision achieved by the CAD system was86.4%.

Authors on paper [79] proposed an algorithm using Fuzzy Neural Network (FNN) to automatically characterize diffused liver diseases. For classification utilizing RUNL, GLDS, FOP, SGLDM and FDTA 12 texture features were taken out. Then again, the features were reduced to six utilizing multiple feature combinations. After that to produce blurry sets and create class edges in a statistical way voronoi diagram of training patterns was built which was utilized by FNN. The Authors showed 82.67% classification accuracy for verification using 150 liver images.

Design made from M-mode motion curve of liver and B-mode US liver picture on the basis of feature extraction by Guohui et.al. [90]. They took out 25 features utilizing M-mode movement curve through GLDS, FOP, RUNL, and a couple of additional extraordinary attributes. After taking out attribute, they used Fisher linear decision rule for choosing 20 helpful features

depending on the minimum classification error. Experiment's outcome divulged that features gained utilizing movement curve were further reasonable for discerning ordinary or cirrhosis, liver in expressions of reactivity and specificity.

For US liver images categorization, Cao et al. suggested different process [91]. For taking out feature SGLDM and FDTA on 64x64 pixels sub-image were utilized by them. In this way the joint feature vector was gained, which was utilized to differentiate 273 sound and 99 fibrosis liver pictures. Fisher linear classifier and SVM (leave-one-out calculation) were utilized. It was found effective in expression of categorization rate. Yet it is proved that the joint feature vector is a bit better.

The authors of paper [92], used an algorithm to recognize diffused liver ailment utilizing Gabor wavelet and categorized ultrasonic liver picture into usual, hepatitis and cirrhosis categories. Familiar three advantages of Gabor wavelets were used by them, which is invariance to swing of picture contents, maximum joint space frequency resolution, and littler feature vector. Attributes were extricated and pictures were categorized into various classes utilizing Gabor wavelet change, dyadic wavelet change, statistical moments and attributes.

Researchers under lead of Bala subramanian suggested a method [93] for automatically categorized benign, malignant, cyst and regular liver pictures utilizing texture attributes via TEM, SGLDM, RUNL, and Gabor wavelets. By manual selection and on the basis of Principle Component Analysis (PCA) on the basis of idea attributes, eight attributes were selected. K-means clustering calculation used by PCA based features whereas physically chosen attributes were categorized by BPN. Finally, it is proved that categorization outcome of BPN were improved than K-means. Poonguzhali et.al., [94] authors classified same liver diseases. The attribute taking out from the ROI of US pictures through Autocorrelation, TEM, Edge Frequency method and SGLDM.

Optimal attribute sets selected from extracted features using PCA. For K-means categorization afterwards optimal features were utilized.

Jeon et al. presented a technique to classify focal liver lesion based on multiple ROI, to obtain more reliable and better classification performance [95]. This technique can be utilized to classify focal liver ailment, for example Hem, Cyst, and Malignancies. From the complete US image the ROI features are extricated at first. Lastly, the categorization of cysts and hemangiomas, categorization of cysts and malignancies, and categorization of hemangiomas and malignancies are classified using the SVM classifier. The preprocessing stage is complicated since it affects the subsequent stages and improves the quality of the images. Their method has shown the overall accuracy of 80%.

Ribeiro et.al., [96] implemented an algorithm using three dissimilar classifiers to classify the different chronic liver ailment. The classifiers utilized are SVM, KNN, and decision tree. The outcome showed that the SVM gained superior performance than the KNN and decision tree classifier. The classification's precision was 73.20%utilizing SVM with a radial basis kernel. Yet, the general accurateness of this process is not high. In another paper [97], the authors given a partly automatic method to categorizing unceasing liver ailment from US liver pictures. For this approach the data, which is collected from laboratories and clinic, are generated by utilized SVM classifier with a polynomial core of the fourth degree. The data achieved 91.67% of sensitivity better than previous approaches. In the coming works, they will extend their method of merging more textural features.

A few more compact summaries of different author's algorithms and accuracy of their proposed technique up to recent years presented in table 1.

Table 1: Summary of various researches on CAD for liver diagnosis

Authors/Year	Number of samples	Features	Classifier	Performance
Fayazul et al ., /2012 [98]	88	Wavelet packet transform	SVM	~95%
Acharya et al., /2012 [99]	100	Wavelet and Higher order spectra feature	DT	93.3%
Jitender et al., /2012 [100]	56	Wavelet packet transform	SVM	88.8%
Jitender et al., /2013 [101]	31	Wavelet packet transform and Gabor Wavelet transform	SVM	98.3%
Jitender et al., /2013 [102]	108	FOS, GLCM, GLRLM, FPS, GWT, TEM	BPNN	87.7%
Jitender et al., /2013 [103]	108	FOS, GLCM, GLRLM, FPS, TEM, Gabor	SVM	87.2%
Nivedita et al., /2014 [104]	42	GLCM	SOM and MLP	81.5%
Jitender et al., /2014 [105]	108	FOS, GLCM, GLRLM, FPS, TEM, Gabor	Neural network ensemble	88.7-95%
Rivas et al., /2015 [106]	7	GLCM	Binary logistic regression	95.45%
Wu et al., /2015 [10]	288	Mean, SD, Kurtosis, Skew	SVM and Random forest	72.81%
Hwang et al., /2015 [107]	115	FOS, GLCM, TEM, Ecogenecity	Baysian regularity learning	96%
Acharya et al., /2016 [11]	100	GIST descriptor	PNN	98%

2.6 Discussion

This chapter proposed in a new way of categorizing and summarizing the different stages of the computerized system scheme applied to ultrasound (US) with focus on liver cancer diagnosis. The up to date review of existing approaches in the literature has been reviewed. To the best of our knowledge, there has been no unique consensus on computer aided diagnosis (CAD) system. Many different algorithms mentioned in the state of art used to find and design optimal solution for automatic liver cancer diagnosis scheme. In our opinion, there should be a trade-off, strengths and weaknesses associated with the choice of the algorithm used for image analysis.

In the future, researchers must pay attention to data pre-processing stage meanwhile minimizing motion artifacts, image noise and tolerable classification time using optimized neural network. It might be possible that integrating multiple effective techniques, potentially improve the general correctness, exactness and techniques concerned to speed of segmentation, also lessening the

quantity of manual interactions of user. Moreover, greater part of the work in the literature concentrated on detection and classification of B-Mode US imaging.

Chapter 3

Speckle Reduction on Ultrasound Liver Images Based on a Sparse Representation over a Learned Dictionary

3.1 Introduction and Contributions of this work

As we discussed in chapter 2 a CAD system carries out the diagnosis in four stages: data preprocessing, image segmentation, feature extraction, and classification [19]. Data preprocessing is the first and most vital step in the CAD system process because it reconstructs an image without eliminating the important features by reducing signal-dependent multiplicative noise called speckle [108].

The development of a precise speckle reduction model is an important step to achieve efficient denoising filter design. Recent review articles [19], [31], reported that speckle reduction filters are categorized into two broad approaches: spatial filtering and multiscale methods. Techniques under spatial domain filtering include enhanced Frost filtering [39], Lee filtering [32], mean filtering [37], Wiener filtering [109], Kuan filtering [42], and median filtering [110]. Spatial filters utilize local statistical properties to reduce speckle noise. However, small details may not be preserved [31]. Several methods [111]–[114] use multiscale filtering, which uses the wavelet transform to preserve the image signal regardless of its frequency content.

This chapter proposes a multiplicative speckle suppression technique for ultrasound liver images, based on a new signal reconstruction model known as sparse representation (SR) over dictionary learning.

Sparse representation provides superior estimation even in an ill-conditioned system [115], and has been found to be very useful in medical imaging applications. However, one challenge of designing this system is the presence of a multiplicative speckle signal because dictionary learning methods are not effective on multiplicative and correlated noise. We overcome this by using two different methods.

Firstly, the speckle noise is transformed into additive noise using an enhanced homomorphic filter that can also capture high and low frequency signal of the image. Secondly, we introduced (TV) regularization of the image and sparse prior over learned dictionaries. Total variation regularization is efficient for noisy image, while the patch-based dictionaries are well adapted to texture features [116], and reduces the artifacts in smooth pixel regions [117].

The advantage of the sparse prior is that it utilizes fewer dictionary columns to reconstruct a noiseless ultrasound image without losing many important features of the signal. Therefore, in our proposed model we combined the two approaches, the patch-based SR over learned dictionaries and the pixel-based TV regularization method, for efficient speckle reduction.

The K-singular value decomposition (KSVD) algorithm [118] is used to learn two modified dictionaries from reference ultrasound image datasets and the corrupted images; these are referred to as dictionaries 1 and 2, respectively. The results are evaluated on both dictionaries and compared with conventional algorithms to show that the speckle noise is suppressed effectively in the ultrasound image using SR.

3.2 Background

3.2.1 Ultrasound noise model

Ultrasound imaging system are often affected by multiplicative speckle [119]. Scattering time differences lead to constructive and destructive interference of the ultrasound pulses that are reflected from biological tissues. Speckle patterns can be classified depending on the spatial distribution, number of scatters per resolution cell, and properties of the imaging system [31]. Speckle noise affects the detectability of the target and reduces the contrast and resolution of the images, making it difficult for a clinician to provide a diagnosis.

In ultrasound, the multiplicative noise models are based on the product of the original signal and noise. Thus, the intensity of a noisy signal depends on the original image intensity. The mathematical expression for a multiplicative speckle model is given by

$$y(i, j) = x(i, j)h(i, j), \tag{1}$$

where $y(i, j)$ is the speckled image, $x(i, j)$ is the original image, and $h(i, j)$ is the speckle noise. The spatial location of an image is represented using indexes i and j, where index i ranges from 1 to N, and index j from 1 to M.

3.2.2 Related work on multiplicative noise reduction

Several algorithms have been proposed to deal with more complex multiplicative and additive speckle noise models [120]. For instance, the Kuan, Frost, Lee filters, and speckle reducing anisotropic diffusion (SRAD) filter [121] are effective on the multiplicative noise model. Other filters, specifically the median, Wiener, and wavelet filters [122], are designed for the additive noise

model [19]. However, each filter has certain advantages and limitations [120]. In a few filter models, the quality of the processed image is affected by the window size: large window sizes cause image blurring, degrading the fine details of an image. Conversely, small window sizes do not denoise the image sufficiently. Other widely used multiplicative noise reduction algorithms are based on the TV regularization term [123], [124], nonlocal methods [125], [126], and wavelet-based approaches [111]. Total variation-based methods effectively remove flat-region-based noise and preserve the edges of images. However, fine details are lost because of over-smoothed textures. Nonlocal algorithms depend on similarities of image patches. Their performance is limited by dissimilar image patches. However, wavelet-based approaches preserve texture information better than TV-based methods. This approach assumes that images in the SRs are based on a fixed dictionary [118], [127]. However, certain characteristics of the processed image might not be captured because the dictionary does not contain any similar image content.

To overcome the above disadvantages, over the past few years, researchers have sought to develop an algorithm based on SR in the field of image and signal processing [128]. This is because the pattern similarities of image signals such as textures and flat regions, mean that the signal can be efficiently approximated as a linear combination using a dictionary of only a few functions called atoms [116], [118], [127]. Elad and Aharon [118] proposed an image denoising algorithm using an adaptive dictionary called KSVD that is based on sparse and redundant representations. It includes sparse coding and dictionary atoms that are updated to better fit the data. The advantage of KSVD compared to fixed dictionaries is that it is effective at removing additive Gaussian noise using the linear combinations of a few atoms, by learning a dictionary from noisy image patches and then reconstructing each patch.

A dictionary $A \in \mathbb{R}^{N_r \times N_c}$, composed of N_c columns of N_r elements, is called a sparse-land model [118]. K-singular value decomposition seeks the best signal representation of image signal y from the sparsest representation α:

$$\hat{\alpha} = \arg\min \|\alpha\|_0 \text{ subject to } \|y - A\alpha\|_2 \leq \varepsilon,$$

where the vectorization of $y(i, j)$ is denoted by vector $y \in \mathbb{R}^{M \times 1}$ and ε is the few number of non-zero entries in α. K-singular value decomposition replaces the dictionary update and sparse coding stages with a simple singular value decomposition. The orthogonal matching pursuit (OMP) method [129] is an effective method to find the sparse approximation. In the OMP, if the noise level is below the approximation, the image patches are rejected. The singular value decomposition constructs better atoms by combining patches to reduce noise for ultrasound speckle reduction. K-singular value decomposition has also proved to effectively reduce the speckle produced by additive white Gaussian noise on corrupted images [118], [127].

The filtering algorithm comprises two steps. First, the dictionary is trained from a set of image data patches or from noisy image patches based on KSVD. The next step uses $\hat{\alpha}$ to compute SR using dictionary A and denoises the image [127].

The method proposed in [130] also uses a dictionary learning approach for denoising ultrasound images. A homomorphic filter is used to convert multiplicative noise into additive white Gaussian noise and then the noiseless signal is reconstructed over image patches (atoms) to create the SR from a learned dictionary. However, noise in flat regions still exists and poor edges make the reconstructed images difficult to analyze. In [116], the authors proposed an image denoising technique that operates directly on multiplicative noise and is based on three terms: SR over an adaptive dictionary, a TV regularization term, and a data-fidelity term. However, the proposed model is nonconvex because of the product between the unknown dictionary and sparse

coefficients and the data-fidelity term is a log function. Therefore, solving the squared l_2 norm is difficult. This optimization problem is overcome by the split Bregman technique. However, these methods do not contain high- and low-frequency components of the image. We obtain this information using an enhanced homomorphic filter designed to improve the final image. Furthermore, we utilize the advantages of combining a TV regularization term and SR learned over two modified dictionaries.

3.3 Sparse Representation Framework for Speckle Reduction

As discussed above, we define our proposed scheme for ultrasound speckle reduction by considering the multiplicative noise model [119] obtained by an ultrasound transducer. Equation (1) can thus rewritten as

$$y_{\partial}(i, j) = x_{\Re}(i, j)n_{\sigma}(i, j), \qquad (2)$$

where $y_{\partial}(i, j)$ is the degraded B-mode image signal [131], $x_{\Re}(i, j)$ represents the ideal image that must be recovered, and $n_{\sigma}(i, j)$ represents the speckle noise, generally modelled as a Rayleigh probability density function with random variables [32], [132]. Each term includes coordinates (i, j) defined according to the acquisition geometry.

In general, a homomorphic filter [133] is a well-proven technique for converting multiplicative noise. In this study, we modified it by taking the log of the multiplicative noisy signal and filtering the image using a Butterworth high-pass (BW-HP) filter to attenuate low frequencies in the transmitted signal while preserving the high frequencies in the reflected component. The equation of the BW-HP filter is

$$H_B(u,v) = \frac{1}{1 + \left[D_0 / \sqrt{u^2 + v^2} \right]^{2f}}, \tag{3}$$

where, D_0 is the cut-off frequency and f is the order of the filter. We varied the frequency values u and v of the i and j spatial coordinates. We used the BW-HP filter because it generates fewer ringing artifacts on the image signal.

We also used a Gaussian low pass (GLP) filter to smooth the low-frequency signal component in the log domain. The equation of the GLP filter is

$$H_G(u,v) = e^{-D^2(u,v)/2D_0^2}, \tag{4}$$

where $D(u,v)$ is the distance from the origin in the frequency plane. Finally, the additive noise signals were estimated by applying inverse transform.

Figure 6 shows the steps used to convert an original noisy image into an image with additive noise using the enhanced homomorphic transform. This technique consists of five steps. We first take the log on both sides of Equation (2) and use a two-dimensional fast Fourier transform (FFT) to represent the image in the frequency domain. Then, the Fourier image is filtered with two filter functions, those are the BW-HP and GLP filters [37]. The BW-HP filter increases the contrast of the image signal corresponding to the high-frequency component. The GLP filter smooths the noise signal without eliminating the entire low-frequency component. Both filtered signals are applied to the two-dimensional inverse fast Fourier transform (IFFT). Finally, taking the exponent of the image, we obtain the transformed image. This process is discussed in detail below.
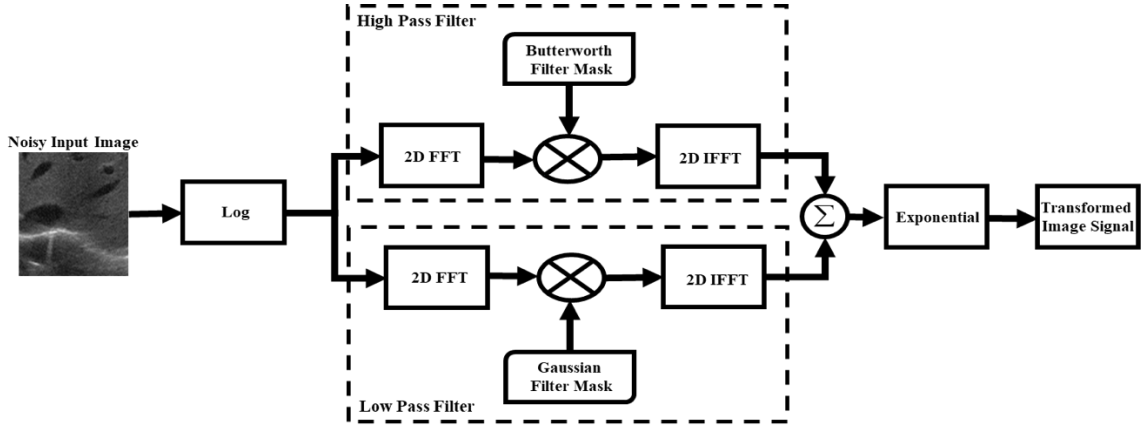
Figure 6. Flow diagram of the enhanced homomorphic filter. FFT: fast Fourier transform; IFFT inverse fast Fourier transform.

Step 1: Take the log on both sides of the $x_{\Re}(i,j)$ and the $n_{\sigma}(i,j)$ signal; now the multiplicative noise can written as

$$\log(y_{\partial}(i,j)) = \log(x_{\Re}(i,j)) + \log(n_{\sigma}(i,j)), \tag{5}$$

After being transformed logarithmically, the signal now contains Gaussian additive noise [134]. We remove $\log(x_{\Re}(i,j))$ from the speckled ultrasound image by applying an additive noise suppression algorithm. Thus, the problem is now to estimate $\log(x_{\Re}(i,j))$ from noisy data.

Step 2: Apply FFT to convert the image into the frequency domain. Equation (5), thus becomes,

$$y_{\partial}(u,v) = F_{x_{\Re}}(u,v) + F_{n_{\sigma}}(u,v), \tag{6}$$

where, $F_{x_{\Re}}(u,v)$ and $F_{n_{\sigma}}(u,v)$ are the FFT of $\log(x_{\Re}(i,j))$ and $\log(n_{\sigma}(i,j))$, respectively.

Step 3: Apply BW-HP and GLP to the $y_{\partial}(u,v)$ by means of two filter function $H_B(u,v)$ and $H_G(u,v)$ from Equations (3) and (4) respectively in the frequency domain. The filtered version of $S(u,v)$ is written as

$$S(u,v) = H_B(u,v)\,y_{\partial}(u,v) + H_G(u,v)\,y_{\partial}(u,v)\,. \tag{7}$$

Step 4: Take the inverse Fourier transform of Equation (7) to get the converted signal in the spatial domain

$$\bar{S}(i,j) = \mathcal{F}^{-1}\{S(u,v)\}\,.$$

Step 5: Finally, we obtain the transformed image $t(i,j)$ by taking the exponent of the image using the following equation

$$t(i,j) = \exp\{\bar{S}(i,j)\}\,.$$

In this paper, we model the transformed image as additive noise degradation $w(i,j)$ of the original image $x_{\Re}(i,j)$, i.e.,

$$t(i,j) := x_{\Re}(i,j) + w(i,j)\,. \tag{8}$$

This completes how we have used the homomorphic filter to transform the speckle noise into additive noise. The two filter functions are utilized to improve edge information by enhancing contrast and smooths the additive noise of the transformed image.

Figure 7 shows the output of the enhanced homomorphic filter at the BW-HP and GLP filter stages. It is clear that the image in Figure 7b has an increased intensity because the low frequency signal is attenuated and the image in Figure 7c is smoothed by the GLP filter. The sum of these two signals is the final transformed noisy image.
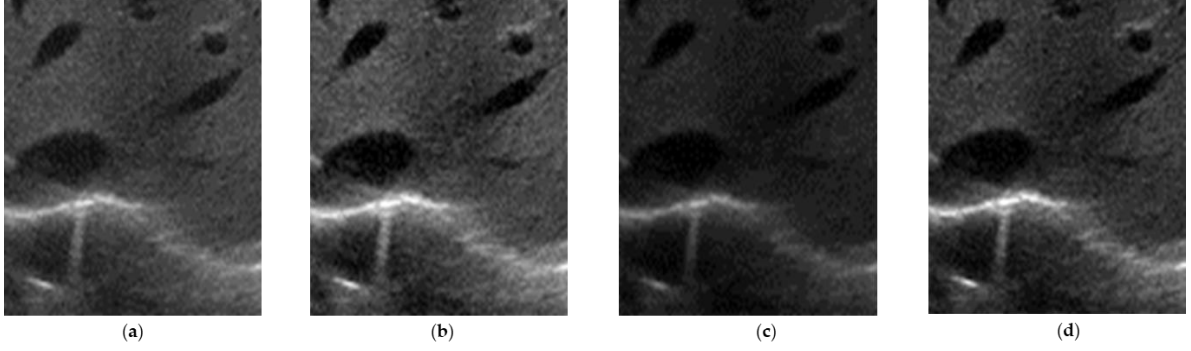
Figure 7. (a) Noisy ultrasound image; (b) Butterworth high-pass (BW-HP) filtered image; (c) Gaussian low pass (GLP) filtered image; and (d) transformed output of ultrasound noisy image.

An ultrasound image $x_{\Re}(i, j)$ can be represented as sparse in the gradient domain. We thus define here a difference signal. A pixel-based TV regularization can be performed on the transformed image for more effective denoising. The horizontal and vertical difference matrices are defined below [135].

$$
V_i x_{\Re}(i, j) = \begin{cases} x_{\Re}(i+1, j) - x_{\Re}(i, j), & if\ i < n \\ 0, & if\quad i = n \end{cases}
$$
$$
V_j x_{\Re}(i, j) = \begin{cases} x_{\Re}(i, j+1) - x_{\Re}(i, j), & if\ j < m \\ 0, & if\quad j = m \end{cases}
$$

Further, the difference signal of $x_{\Re}(i, j)$ is defined as

$$
V_{i,j} x_{\Re}(i, j) = \begin{pmatrix} V_i x_{\Re}(i, j) \\ V_j x_{\Re}(i, j) \end{pmatrix}.
$$

We can show that there exists a dictionary $A \in \mathbb{R}^{N_r \times N_c}$ with which the original image can be sparsely represented as

$$
x_{\Re} = A\alpha ,
$$

where $x_{\Re}$ is the vectorization of the recovered signal $x_{\Re}(i, j)$ such that $x_{\Re} \in \mathbb{R}^{N_r}$. If a signal $x_{\Re}$ is K-sparse in the dictionary $A \in \mathbb{R}^{N_r \times N_c}$ for $N_c > N_r$, we imply that the signal can be represented

with K columns of the dictionary. The column vector $\alpha \in \mathbb{R}^{N_c \times 1}$ is the vector of the coefficients. Then, by optimizing the following convex problem, the signal $x_\Re$ can be recovered:

$$
\begin{aligned}
&\min \|\alpha\|_0, \\
&\text{subject to } \|t - A\alpha\|_2^2 \leq \varepsilon.
\end{aligned}
\tag{9}
$$

In Equation (9), a $NM \times 1$ column vector t is the vectorization of the transformed image $t(i, j)$, note that $NM = N_r$. Also note that ε is a utility parameter selectable according to the noise strength. This convex constrained problem can be transformed into an unconstrained optimization problem using the Lagrange multiplier method [136]:

$$
\min \|t - A\alpha\|_2^2 + \tau \|\alpha\|_0.
\tag{10}
$$

Using the unconstrained problem, we are able to combine a regularization term, which is weighted by parameter $\tau > 0$ and a quadratic data-fidelity term. Equation (10) is not ready for use yet since we do not know the sparsity dictionary A. Therefore, we use the following approach where the dictionary, the sparse representation coefficient vector α, and the image vector $x_\Re$ are estimated altogether. The overall optimized discrete sparse model proposed in this paper, for denoising the ultrasound image, can be written as

$$
\left\{\hat{x}_\Re, \hat{\alpha}_{ij}, \hat{A}\right\} = \min_{x_\Re, \alpha_{ij}, A} \lambda \|Vx_R\|_1 + \tau \sum_{ij} \|R_{ij}t - A\alpha_{ij}\|_2^2 + \tau \sum_{ij} \|\alpha_{ij}\|_0,
\tag{11}
$$

where R_{ij} is an operation that extracts a square image patch from the transformed image t located at the i, j pixels of the image. The notation $\|.\|_1$ is used to imply the l_1 norm, which is the sum of the absolute values of the argument signal, which in this case is the difference signal Vx_R. There are two positive parameters λ and τ used to balance the contribution of different terms. In

Equation (11), the first and second terms are the TV regularization norm and the sparse representation prior. Optimization in Equation (11) seeks to find a solution with which each patch of the recovered image can be represented by a dictionary matrix with sparse coefficient α in the sense of a bounded error. The l_0 norm gives the sparsity constraint which controls the sparsity coefficients of any small image patch.

As mentioned in Related Work Section 2.2, there is a sparse coding stage that utilizes the KSVD iterative process. In the first stage, sparse coding is performed assuming fixed $x_\Re$ and A. In the second stage, dictionary A is updated to minimize using known sparse coefficients α and $x_\Re$. The sparse coefficients $\widehat{\alpha}_{ij}$ are computed using the OMP method [137] because of its efficiency and simplicity. Elad et al. [127] showed that learning a dictionary trained from good quality image patches and noisy images results in better performance.

In this paper, we use two approaches to train the dictionary. The first approach is to use a group of image patches taken from many ultrasound reference images. We call the dictionary obtained from this approach Dictionary 1. The second approach is to use the corrupted images and call them Dictionary 2. We aim to compare the performance difference based on these two approaches. The comparison is made in the Results section.

It should be noted that Equation (11) is non-convex because of the non-differentiable TV regularization term and the product of the unknowns A and α_{ij}. We overcome this by using the split Bregman iterative approach [138].

Overall, the proposed algorithm can be summarized as follows:

1. Convert the multiplicative noise into additive noise using an enhanced homomorphic filter and capture the high- and low-frequency components to retain detailed information.

2. Apply pixel-based TV regularization to smooth the filtered image signal.

3. Apply patch-based sparse representation over a dictionary trained using the KSVD algorithm. We employed two modified dictionaries—one trained with a set of reference ultrasound image patches and another trained using the speckled image patches.

4. Iterate between the TV regularization and sparse representation procedure to improve the reconstructed image.

Figure 8 summarizes the proposed algorithm.

The reconstructed denoised image using the proposed algorithm were compared with the original image. Two image quality metrics were used for quantitative performance measurements: peak signal-to-noise ratio (PSNR) and mean structural similarity (MSSIM) [139]. Peak signal-to-noise ratio is defined as:

$$PSNR = 10 \log_{10} \frac{N_{max}}{\frac{1}{MN} \sum_{n=1}^{N} \sum_{m=1}^{M} |x(n,m) - \hat{x}(n,m)|^2} \, , \tag{12}$$

where N_{max} represents the maximum fluctuations in the input image. Here, $N_{max} = (2^n - 1)$, $N_{max} = 255$, when the components of a pixel are encoded using eight bits. N denotes the number of pixels processed, $x(n,m)$ is the original signal, and $\hat{x}(n,m)$ is the recovered image signal. In *MSSIM*, the structures of the two images are compared after normalizing the variance and subtracting the luminance as follows:

$$MSSIM = \frac{1}{N} \sum_{i=1}^{N} \left[l(\hat{x}, x) \right]^{\alpha} \cdot \left[c(\hat{x}, x) \right]^{\beta} \cdot \left[s(\hat{x}, x) \right]^{\gamma} , \tag{13}$$

where $l(\hat{x}, x)$ denotes luminance, $c(\hat{x}, x)$ denotes contrast, and $s(\hat{x}, x)$ denotes structure

comparison functions. Further, $\alpha, \beta,$ and r are weighted parameters that are used to adjust

the relative importance of the three components.
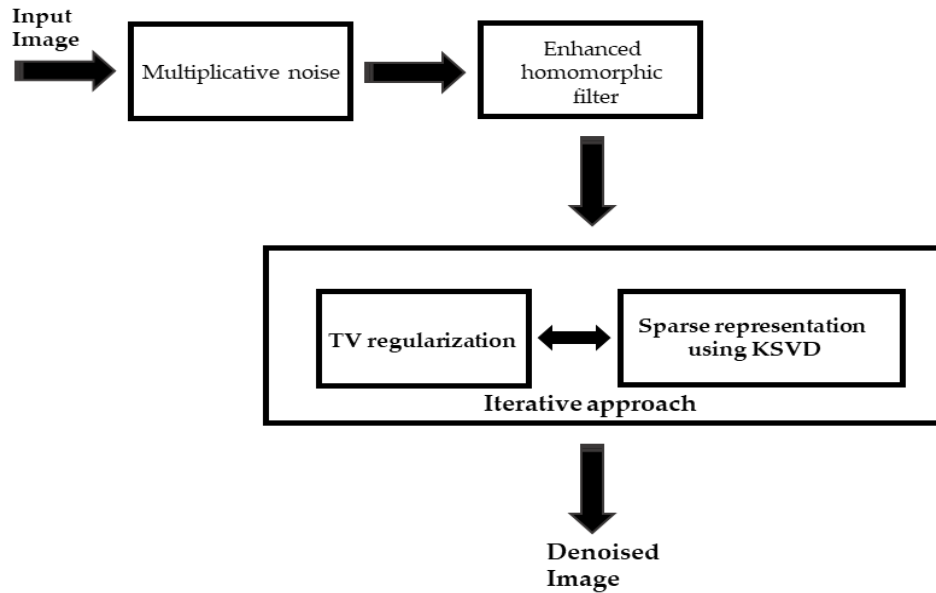
Figure 8. Proposed despeckle model for an ultrasound image. KSVD: K-singular value decomposition.

3.4 Experimental Results and Discussion

3.4.1 Simulations on Synthetic Images

In this section, we analyze the performance of the proposed approach on the synthetic Shepp–

Logan phantom test image [140] (Figure 9a) with a speckle noise variance of $\sigma = 10$ (Figure 9b)

of a 256×256 pixel size. This result helps us to understand the effectiveness of the simulated

image, clearly determine the distinctive features of the image, and optimize the algorithm before

testing on the clinical datasets. We compared the proposed algorithm with some standard speckle

reduction filters for ultrasound liver images [19]. The compared algorithms were local statistical

filters such as the Frost filter [39], Lee filter [32], 3×3 Weiner filter [109], Kuan filter [42], 3×3

median filter [110], and speckle reducing anisotropic diffusion (SRAD) filter [121]. In addition,

multiscale filters such as wavelets [122] were evaluated. The despeckled images in Figure 9e–g show that the Frost, wavelet, and Kuan filters do not effectively reduce noise. In contrast, Figure 9h–j show that the median, Weiner, and SRAD filters, reduce most noise; however, the edges are not preserved and artificial noises can be introduced to a certain extent. This result verifies that the proposed SR technique reduces noise and preserves the edges better than the conventional methods on synthetic images. Table 2 shows the PSNR value and MSSIM value. The proposed algorithm reconstructs the original image with a PSNR value of 36.86 dB with Dictionary 1 and 37.04 dB with Dictionary 2.
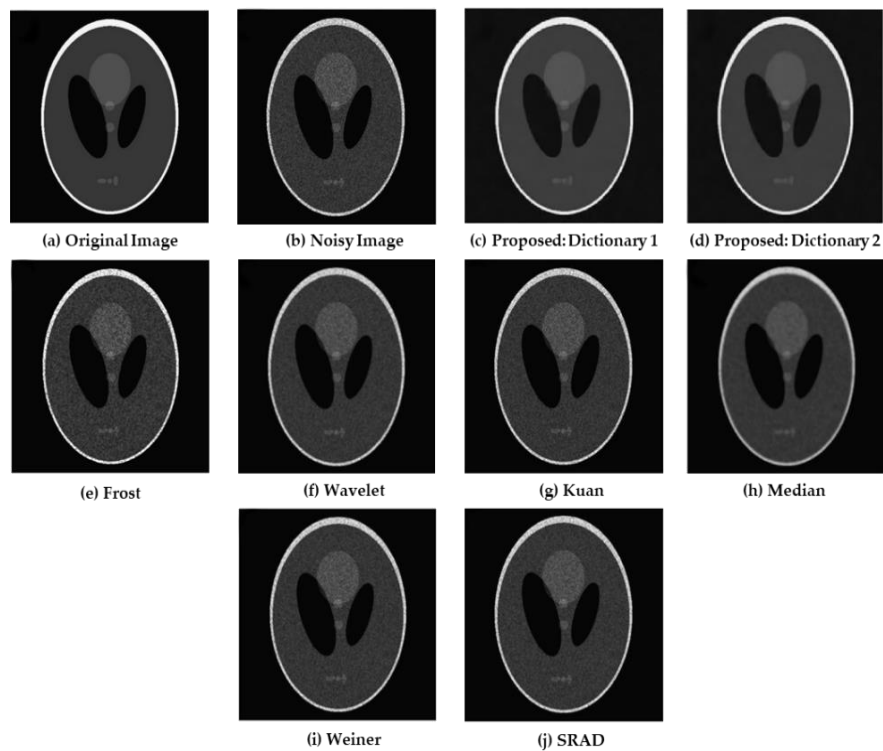
Figure 9. (a) Original image; (b) noisy image. Results of the proposed method with (c) Dictionary 1 and (d) Dictionary 2; Results of the (e) Frost; (f) wavelet; (g) Kuan; (h) median; (i) Weiner; and (j) speckle reducing anisotropic diffusion (SRAD) filters.

Table 2: Peak signal-to-noise ratio (PSNR) and mean structural similarity (MSSIM) for the synthetic images for $\sigma = 10$.

Models	PSNR (dB)	MSSIM
Noise image	32.113	0.727
Frost	32.466	0.768
Wavelet	33.214	0.801
Kuan	32.895	0.794
Median	34.597	0.839
SRAD	33.434	0.827
Weiner	33.782	0.834
Proposed: Dictionary 1	36.862	0.953
Proposed: Dictionary 2	37.044	0.967

3.4.2 Clinical Liver Ultrasound Images

The proposed algorithm efficiency was estimated using a set of B-mode greyscale ultrasound liver images. The images were obtained using the ECUBE 12R ultrasound research system from Alpinion medical systems, Seoul, Korea. The components used to generate the ultrasound images include a 128-element linear transducer at a center frequency of 5 MHz, a lateral beam width of 1.5 mm, and a pulse length of 1 mm. In our experiment, sparse coding was performed using two dictionaries with a 64×256 size, designed to handle patches of 8×8 size pixels ($N = 64$ and $K = 256$)—one trained from a noisy image and the other trained from a set of reference images.

The training data were constructed from a dataset comprising 3245 reference ultrasound images. The random collection of 16×16 dictionary atoms ($K = 256$) is presented in Figure 10a and the dictionary trained on the noisy image itself by overlapping patches is represented in Figure 10b. Where, every dictionary atom occupies a cell of 8×8 pixel ($N = 64$). We performed the tests on the three ultrasound reference images shown in Figures 11a, 12a and 14a. The KSVD algorithm was initialized with a trained dictionary and executed 180 iterations, as recommended in [127].
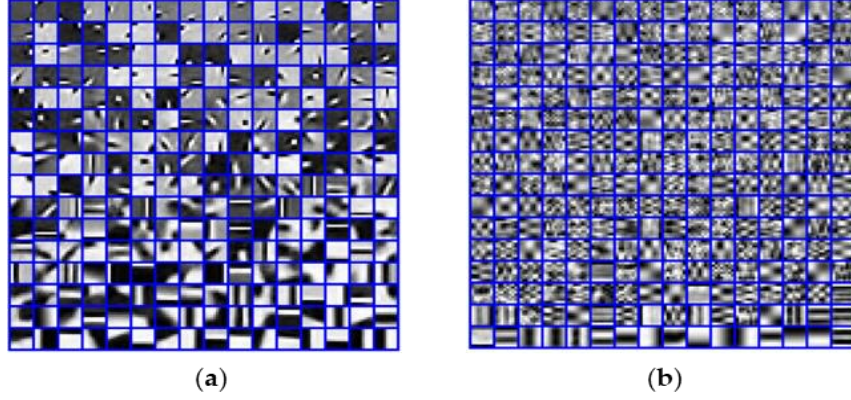
Figure 10. The random collections of 16×16 atoms ($K = 256$) of trained dictionary from (a) a reference set of 3245 ultrasound images and (b) a noisy image.

The numerical evaluation was performed using PSNR and MSSIM (as discussed in subsection 3.1) on the proposed algorithm and compared with the denoising methods Frost filter [39], Lee filter [32], 3×3 Weiner filter [109], Kuan filter [42], 3×3 median filter [110], SRAD filter [121], and wavelet filter [122]. Figure 11a, shows a right lobe liver image with size 256×256 pixels, where the lateral size is given by the *x*-axis, and the axial size is given by the *y*-axis. In this original image, we included a speckle noise parameter $\sigma = 10$ and the PSNR was calculated using Equation (12). It is clear that detailed information of the image is highly distorted, as shown in Figure 11b with a PSNR value of 28.148 dB. Figure 11c,d show the denoising results obtained by the proposed method using Dictionary 1 with a PSNR value of 35.033 dB and Dictionary 2 with a PSNR value of 35.537 dB. It is clear that the SR over learned dictionaries improves both edges and smooth features by eliminating the noise and reconstructs the image as much closer to the original image, as shown in Figure 11a.
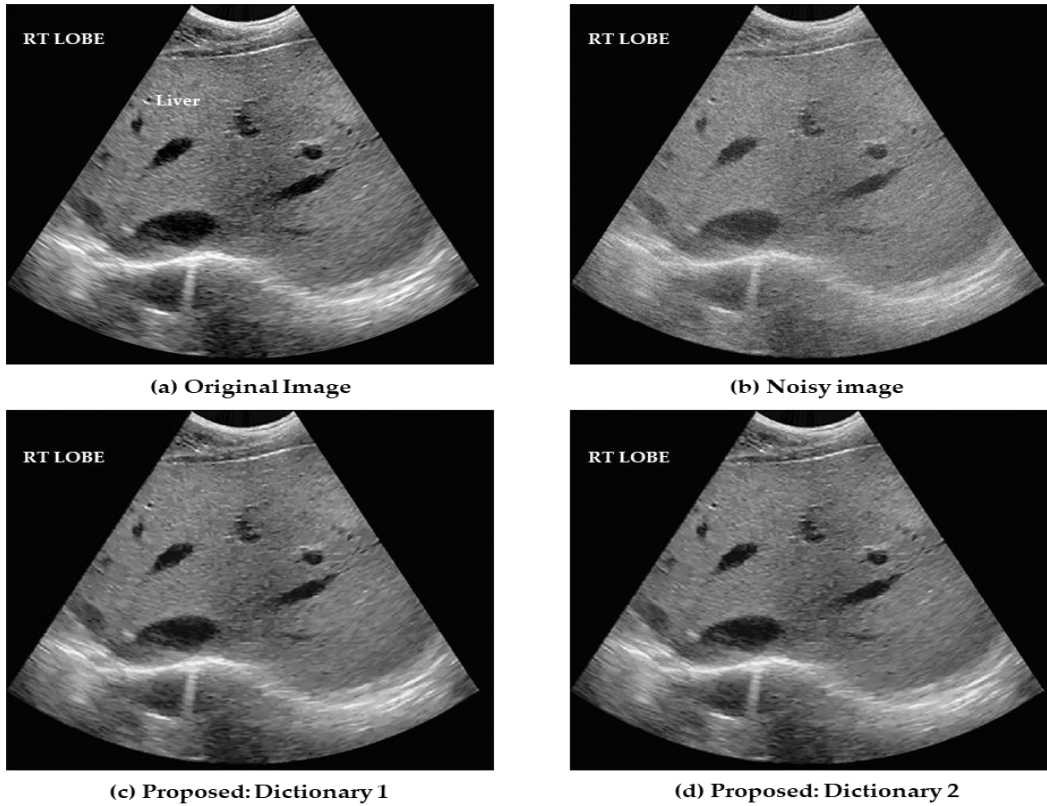
Figure 11. Reconstruction of liver right lobe images. (a) Original ultrasound image; (b) Speckled ultrasound image (PSNR = 28.148 dB); Images reconstructed using (c) Dictionary 1 (PSNR = 35.033 dB) and (d) Dictionary 2 (PSNR = 35.537 dB).

Figure 12 shows the comparative experimental results obtained on real-time ultrasound images. For this experiment, we obtained a 256×256-pixel liver image of a healthy person with a PSNR value of 24.6271 dB. The radio frequency (RF) frames were obtained using a linear transducer with a frequency range of 8 MHz. This frequency range was selected because of its suitability for liver imaging, and we considered natural speckle noise for these experiments. The original speckled image was then denoised using the proposed algorithm with both dictionaries and also using conventional algorithms. To assess the speckle reduction, we selected two regions in of the speckled image. The two regions in the case of Figure 12a are displayed as a red square and a green square. The red one indicates the diaphragm of a liver and the green square shows the presence of an excessive noisy region observed from deeper tissue. The differences can be noticed

from the filtered images in dashed red and the green square. Figure 12d–f show that detailed information lost by the blurring effect on the results obtained with Frost filter, median filter, and Kuan filter. In particular, the wavelet filter, Weiner filter, and the SRAD filter are not very effective in reducing speckle and perform poorly in retrieving sharp edge information, as can be seen in Figure 12g–i. Figure 12b shows the results for the proposed method using Dictionary 1 (PSNR = 30.3345 dB) and Figure 12c shows the results for the proposed method using Dictionary 2 (PSNR = 30.8073). It is clear that the image denoised using the proposed SR method reconstructed image very close to the original image. It can also be seen that the dictionary trained on the noisy image gives better results than using a set of multiple references images. The results of this comparative experiment show that the proposed algorithm not only reduces the speckle noise but also preserves the edge information. Table 3 shows the PSNR and MSSIM values to quantify the results numerically for noise parameter $\sigma = 15$.

Speckle is an arbitrary granular texture noise that degrades ultrasound image quality. This experiment was performed to evaluate different noise variances by comparing the PSNR obtained using the proposed algorithm and other despeckling algorithms. The simulated result using the noise levels 10, 15, 20, 25, and 30 are illustrated in Figure 8. The results clearly depict that, for different noise variances, the proposed algorithm gives the best PSNR value of all the algorithms on speckle reduction.
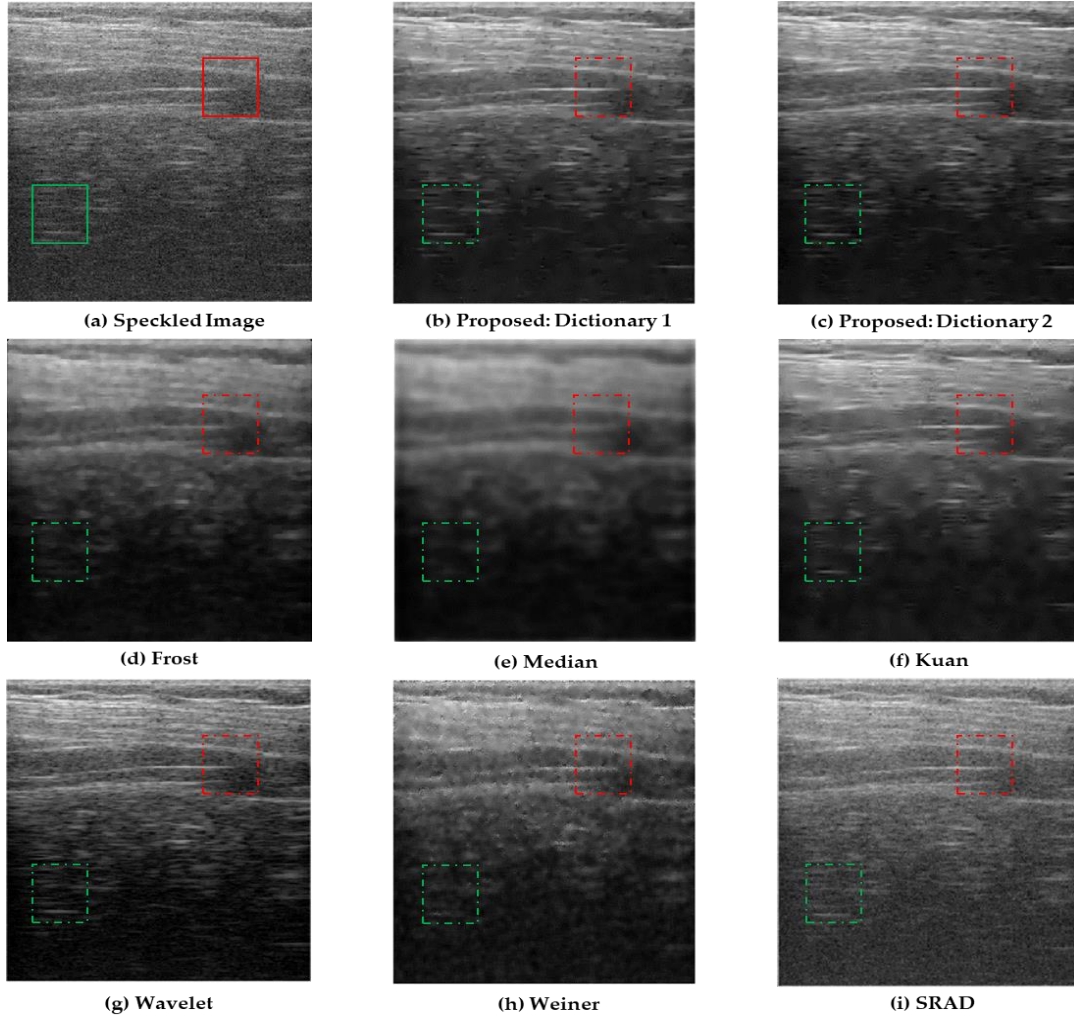
Figure 12: Despeckled results obtained for the ultrasound liver dataset using a linear transducer with a frequency of 8 MHz. The red and the green boxes highlight the differences observed from the noisy and filtered images. (a) Speckled image and results yielded by the proposed method using (b) Dictionary 1 and (**c**) Dictionary 2 as well as results using the (d) Frost; (e) median; (f) Kuan; (g) wavelet; (h) Weiner; and (i) SRAD filters.

Table 3. PSNR and MSSIM for the ultrasound liver image for $\sigma = 15$.

Models	PSNR (dB)	MSSIM
Frost	28.966	0.822
Median	25.497	0.659
Wavelet	27.772	0.782
SRAD	28.766	0.813
Kuan	28.279	0.801
Weiner	29.218	0.834
Proposed: Dictionary 1	30.334	0.901
Proposed: Dictionary 2	30.807	0.926
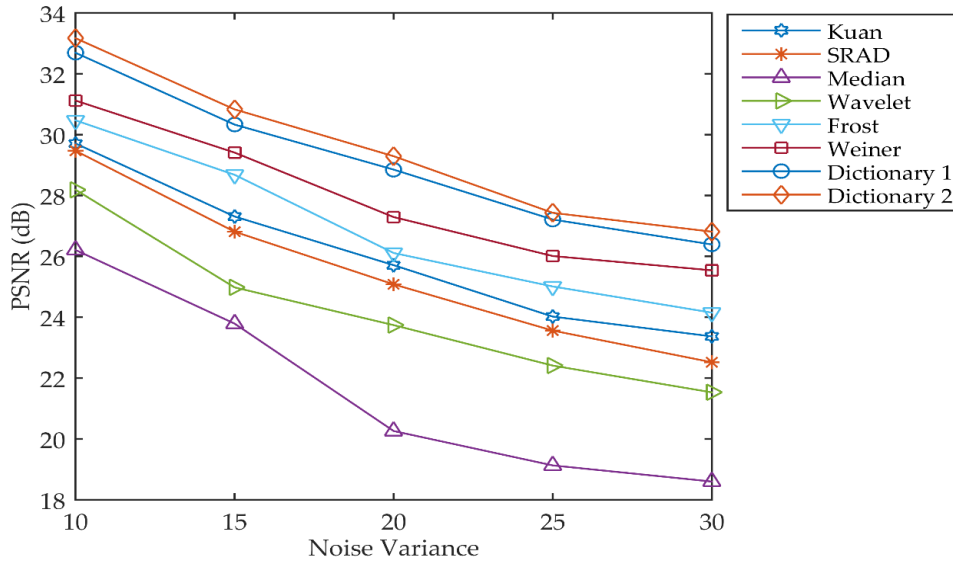
Figure 13: Comparison of PSNRs obtained by different methods. SRAD: speckle reducing anisotropic diffusion.

The experiments presented above were performed on ultrasound liver images, and the performance compared with conventional methods. However, our algorithm can also be utilized for a wide range of ultrasound images. To prove this, we conducted experiments on a real thrombus (blood clot) image with a left ventricular mass [141]. The visual assessment was performed using the proposed technique and the results compared to those obtained by various other algorithms. The reference image size was 256×256 pixels in order to fit our proposed model. The data were obtained from an open medical imaging dataset on GitHub [55]. The ultrasound image along with a marked note are shown in Figure 9a. The dashed white box in Figure 14b–j indicates regions of the ventricular mass. The thrombus data-set results presented in Figure 14h–j show that the wavelet, Weiner, and SRAD filters performed very poorly in noise reduction. The difference can be seen from the white note marked on the right atrium of the reference ultrasound image in Figure 14a. Figure 14e–g shows that Frost, median, and Kuan reduces speckle but tends to over-smooth the image, which leads to the loss

of a distinctive feature of the unclear mass. Among all the methods, Figure 14c,d show good results for the SR-based on learned dictionaries 1 and 2. Several details are well preserved and the speckle noise is reduced efficiently. Figure 15 shows the zoomed sub-images of Figure 9 to observe a clear visualization of the despeckled images. The red box highlights the texture details in the noisy image and the filtered image for a comparative visual assessment. It can be noted that from the Frost, Median, and Kuan filtered data displayed in Figure 15d–f, an unclear mass (blood clot) and texture feature are blurred and over smoothed. Figure 15h,i show that the Weiner and SRAD filters are not much more effective on speckle reduction. These filters also greatly reduce the contrast, making images more indistinguishable from the background. This effect is especially noticeable in the case of the Wavelet filter as shown in Figure 15g. It was found that the anatomical structure was more clearly visible in Figure 15b,c obtained using the SR framework, where the speckle is reduced around the unclear mass without removing its features such as edges and texture. These results were comparatively better than those of Figure 15d–i of the standard despeckling methods. Thus, the proposed algorithm has various advantages for use in CAD systems based on image analysis, such as segmentation and edge detection. Future work will include extensive laboratory and clinical testing on diseased and healthy subjects for a more rigorous validation of the system. In conclusion, our approach reconstructs the detailed information in real ultrasound images, not only by preserving edge information but also by eliminating artifacts and reducing speckle noise.
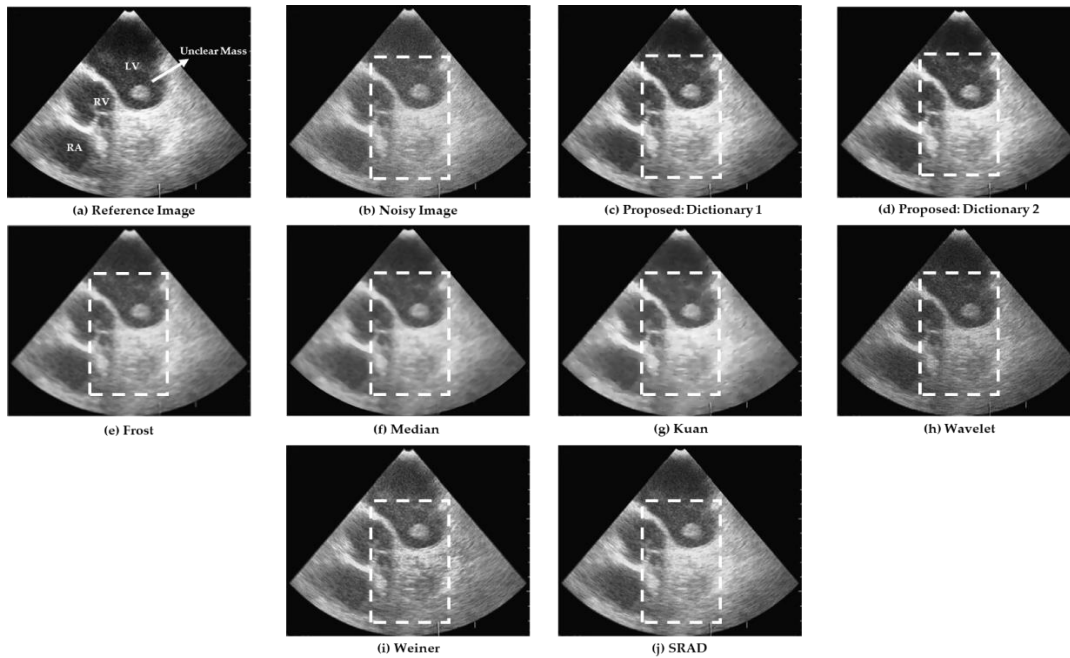
Figure 14: (a) Ultrasound image of the thrombus in the left ventricle. LV: left ventricle, RA: right atrium and RV: right ventricle and (b) noisy image. Despeckled ultrasound images of proposed method using (c) Dictionary 1 and (d) Dictionary 2. Results using the (e) Frost, (f) median, (g) Kuan, (h) wavelet, (i) Weiner, and (j) SRAD filters. The dashed white box indicates the region of image showing visual enhancement owing to despeckling.
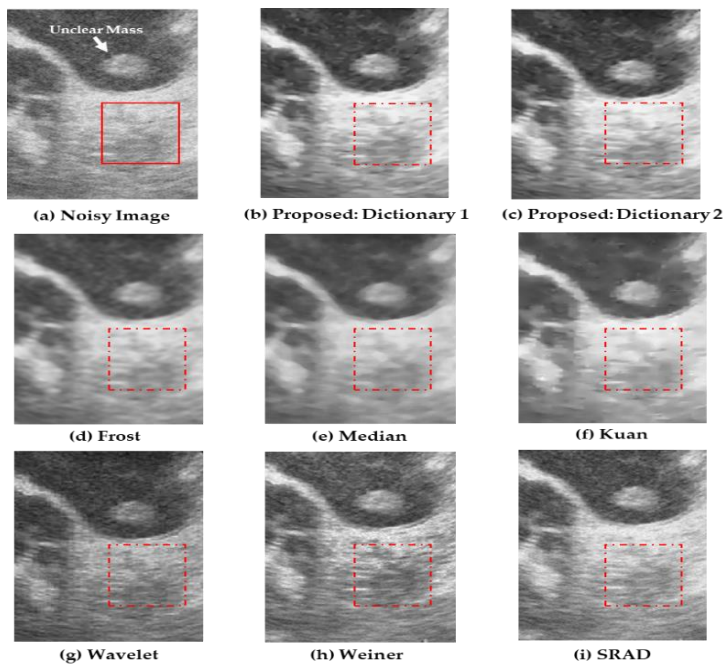
Figure 15: (a) Zoomed sub-image of noisy thrombus ultrasound images. The red boxes highlight texture details of images for visual assessment. Results of proposed method using (b) Dictionary 1 and (c) Dictionary 2. Results using the (d) Frost; (e) median; (f) Kuan; (g) wavelet; (h) Weiner; and (i) SRAD filters.

3.5 Conclusion

In this chapter, we presented a method that reconstructed ultrasound images by suppressing multiplicative speckle noise using the SR framework. The proposed method utilizes an enhanced homomorphic filter, TV regularization, and sparse prior over two learned dictionaries. In addition, the KSVD algorithm is used to train the two dictionaries—one trained with a set of reference ultrasound image patches and another trained with the speckled image patches. Both training options were tested with the synthetic images and various clinical ultrasound images. The experimental results obtained for different noise levels proved superior to those of other standard denoising methods. The results also show that the two modified dictionaries performed well with sparse and TV regularization terms. Overall, the proposed SR framework reconstructs the image signals by removing speckle noise while preserving the texture and yielding a smoother image than conventional methods without eliminating edges.

Chapter 4

Blockchain-Based Distributed Patient-Centric Image Management System

4.1 Introduction and Contributions of this work

Transition to electronic management of health records has necessitated practitioners and their patients to make use of several new acronyms such as electronic medical records (EMRs), electronic health records (EHRs), and personal health records (PHRs) [142]. These health records usually contain medical images and patient information, such as physician name, personal statistics (e.g., age and weight), home monitoring device data, and other data processed by practitioners in a text format. According to the HIPAA privacy rule [143], providers are allowed to respond up to 30 days after a patient request to perform an update or removal of medical records added erroneously. Medical images and patient information are stored and maintained by different hospitals, even when being related to the same patient. This increases the volume of data and leads to a phenomenon of big data. A digital watermarking technique is employed to reduce the storage and transmission overhead by interleaving patient information with medical images [144]. However, this method provides only a basic framework and does not consider introducing security measures to address concerns about data manipulation over cross-domain networks. Current technologies for transferring medical images and patient information are deployed on centralized data centers that are deemed inappropriate due to privacy, accessibility, storage, and security concerns [145]. Over recent decades, medical record data breaches within large medical data centers create additional difficulties for all companies seeking to develop medical image

processing applications [146].

Recently, the blockchain technology (e.g., Bitcoin [147] and Ethereum [148]) has become one of the most important research topics, not only in the finance industry but broadly across the field of information technologies due to its decentralized nature. Healthcare-based blockchain applications have been gaining particular attention in terms of applying them to enable interoperable sharing the real-time data between providers, payers, and patients [17], [149].

Public blockchain technology is an open distributed ledger that stores all transaction details in blocks [6]. A typical blockchain consists of a directed acyclic graph (DAG) structure, where each block is linked with the previous block by a hash. Information stored in each block is public and cannot be easily deleted or modified. Therefore, a blockchain is considered to be a decentralized method to facilitate verifiable exchanges of transactions between any two entities efficiently and permanently. Timely verification and recording of transactions are possible without the necessity in a centralized intermediary. A blockchain has such advantages as being tamper-proof and capable of protecting information against integrity-based attacks.

A significant problem with regard to storing medical images and records in a blockchain is the size of the content. For example, as of October 2019, the size of the Bitcoin blockchain reached 286.23 GB[1]. This is the result of data accumulation over the past ten years at a growth rate of 1 MB every 10 minutes since Bitcoin was launched in 2009. There are approximately 1000 transactions in a block. Thereby, a single transaction has the order of 1 KB. The size of medical images corresponds to the orders of magnitude larger than those a public blockchain can offer [18]. To solve the problem of decentralized storage, the Protocol Labs [150] created a distributed web called Inter Planetary File System (IPFS). IPFS was designed to enable a content-addressable,

---

[1] [online]. Available: https://bitinfocharts.com/bitcoin/

peer-to-peer (P2P) technology to share and store hypermedia in a distributed file system. Several other decentralized storage systems were developed, such as *storj, swarm,* and *sia* [151]. IPFS has an advantage of being compatible with other blockchain networks by offering an off-chain storage solution. IPFS provides permanent, smarter, and faster web services to distributed data access systems.

However, several obstacles exist in terms of storing sensitive medical images over these distributed storage solutions, such as unauthorized access and privacy concerns with regard to patient images. Namely, the ability to manage big data across general practitioners, hospitals, patients, and medical institutes without significant exposure to the risk of privacy breaches is essential. Another important aspect of a confidential and secure storage system is the ability to reduce the cost and restrictions of medical image acquisition by eliminating the need in centralized parties [152].

Therefore, the following research question is formulated:
"How can we design a patient-centric distributed architecture for the purpose of medical image storage and sharing, while simultaneously addressing the concerns about privacy, security, access flexibility, and costs?"

To answer this question, we propose a proof-of-concept (POC) design for a distributed framework called a patient-centric image management (PCIM) system that is a blockchain-based architecture designed to facilitate secured patient-centric access and storage of encrypted medical images within an open distributed network.

The contributions of this paper are as follows:

(1) We provide a brief overview on the structure of the proposed PCIM system and illustrate interactions among different components of the system.

(2) We propose a patient-centric access control protocol using a smart contract (PCAC-SC). Specific functions are considered to transmit information in and out of the Ethereum blockchain and give access privileges between entities.

(3) We implement a framework to test feasibility of the concept. To this end, we have developed a PCAC-SC prototype on an Ethereum test network. We have published the related source codes online.

(4) We verify the functionality using test cases and analyzed the capabilities of the proposed framework.

4.2 Related work

The practice of medical health record registering and sharing has changed considerably in the past 20 years, largely because of strict practice standards, the use of complex technologies, and accurate diagnosis and treatment. Medical images are typically shared on CDs or DVDs shipped between hospitals, physicians, and patients to conclude on diagnosis, however, applying this technology might lead to damage or interception of medical images resulting from patient or physician errors [14]. To overcome the shortcomings of physical media transfer, a cloud-based technology was introduced to share, archive, and store medical images across various healthcare enterprises, usually in an format called digital imaging and communications in medicine (DICOM) [15],[16]. The electronic transmission of medical images was developed by the Radiological Society of North America (RSNA) based on the image-sharing network (ISN) [153]. However, the ISN architecture employs centralized image storage, where images are indexed by a cryptographic hash managed by a third-party clearing house implemented in the cloud. Patients can authorize health care providers to access their images using a PHR. Physicians can view unencrypted images and conclude on a diagnosis using an edge server at each local radiology site. The edge server uses

a key technology called a picture archiving and communication system (PACS) [154], which is aimed to provide economical storage and convenient access to images obtained from different medical imaging modalities, such as ultrasound (US), mammograms, X-ray, magnetic resonance imaging (MRI), and computerized tomography (CT) [155].

In 2006, the publicly funded National Health Service (NHS) in England employed a national broadband network service called N3 (the National network) to connect all NHS National programs in IT (NPfIT), such as the NHS care records service, electronic medical prescriptions, and NHS-PACS [156], [157]. A high-speed IP-based virtual private network (VPN) was used by N3 to communicate between hospitals and general practitioners. However, N3 was preceded by the Health and Social Care Network[2] that went live in April 2017 to provide a reliable, efficient, and flexible method for health care organizations to access, process, and exchange electronic information. Although the current state-of-the-art with regard to medical image sharing does not require physical media transfer, the infrastructure robustness relies on third-party intermediaries and centralization of the network.

Several hospitals and research facilities use PACS to store and access medical images obtained from various modalities to provide patient care from different locations [158], [159]. Researchers from the leading cybersecurity company McAfee have found that poor security may lead to exposure of the medical data to cybercriminals [160]. The researchers determined that more than 1,100 PACSs were directly connected to the Internet without the recommended layer of network security or VPNs. After the investigation, it was found that default accounts, cross-site scripting, and vulnerabilities in the web server could lead to breaches in PACS access and permanent modifications of medical images. The existing infrastructure design raises concerns regarding the

---

[2][Online]. Available: https://digital.nhs.uk/services/health-and-social-care-network

use of third-parties and a centralized network. Consequently, it is important to design a proper network that considers a decentralized architecture seeking to implement a widespread secured image-sharing system.

Recently, several researchers focused on developing a framework that combine a cloud service and a blockchain for the purpose of medical health record sharing. In [161], the authors designed a breadcrumb mechanism for a medical record search known as MedBlock. Breadcrumbs were aimed to record addresses of blocks containing the patient-related data. Unfortunately, these solutions are not applicable to the process of searching the data over the blockchain due to an increase in the fragmented data. The authors in [5] proposed MedShare, a hybrid cloud-based sharing solution for EHRs that is based on a centralized cloud server provider. Then, this external server was replaced by two decentralized networks called MedChain [162]. In the concept of MedChain, the authors proposed a session-based data sharing scheme and a digest chain structure implemented using an immutable blockchain and the mutable P2P storage architecture. However, the possibilities of tampering and manipulating stored patient health records are at high risk due to the mutable P2P storage architecture. In [163], a blockchain-based cross-domain image-sharing framework was proposed. However, no attempt to address privacy concerns has taken to facilitate sharing images through a blockchain.

4.3 System Components

In this section, we present the description of main components represented in the proposed PCIM system.

4.3.1 Ethereum blockchain

Ethereum [7, 28] was developed based on the Bitcoin system and incorporated a programmable smart contract (SC) platform. In other words, SC is a computer program that stores rules for

negotiating the terms of a contract. Programs can autonomously verify and execute contract-related agreements, thereby, reducing the cost of constructing and managing a centralized database. SC employs the Ethereum virtual machine that allows users to run SC within the blockchain network. In general, the fee mechanism of the Ethereum system depends on the value of gas [148]. A certain amount of gas is required to execute a SC and perform a transaction. A digital currency can be used to purchase gas. The actual transaction cost is defined as follows:

$$ether = gas\ used \times gas\ price.$$

The Ethereum platform consists of two types of accounts: external owned accounts (EOAs) controlled by private keys and contract ones controlled by the contract code. EOAs are used to execute a transaction sending ether or to trigger execution of SC. An Ethereum transaction includes such parameters as the recipient address, gas price, gas limit, ether values transferred, account nonce, sender signature, location of the medical image, and other additional image characteristics. The Ethereum blockchain has an associated state database based on a Merkle-Patricia tree structure that can be emulated using IPFS objects. Therefore, we can model a blockchain using IPFS for off-chain and on-chain storage of medical images. In the proposed scheme, we implemented the PCAC-SC protocol using an Ethereum blockchain to enable transparent controlled access, so that malicious entities could not access the medical images without patient authorization.

4.3.2 IPFS storage

IPFS is a content-based peer-to-peer (P2P) protocol in which each medical image file is assigned with a unique fingerprint denoted as a cryptographic hash. Addressing the hash is applied to make the contents immutable [150]. The IPFS file storage structure consists of a Merkle DAG that combines Merkle trees with a DAG. The key feature of IPFS in terms of the proposed system is to access medical images through the content addressing approach, rather than location-based

addressing one. Therefore, IPFS allows reducing the bandwidth cost, increasing the image download speed, and distributing a large volume of data with no duplication, in which allows achieving storage savings. The data structure for storing a file is an IPFS object, which consists of data and links. A single IPFS object can store up to 256 Kb of the unstructured binary data. If a file is larger than 256 Kb, it is split into and stored as multiple IPFS objects with an empty object containing links to all other objects of the image. Therefore, IPFS is an immutable storage mechanism; modifying a file will change the hash value. To update a file, IPFS uses a version control system called Git[3], which creates a commit object, when a file is added to the IPFS network; this approach allows tracking all file versions. When an update is made to a file, a new commit object is created as a link to a new object to interconnect with an older commit object version of that file.

The default installation of IPFS connects the local machine to the global distributed network. Whereas in this case any peers can retrieve images using a cryptographic hash value, in the proposed framework, we overcome this problem by encrypting sensitive medical images before uploading them.

4.3.3 Securing medical images

At present, the storage of medical records is fragmented [165]. The private information of a patient such as age, name, and diagnostic summary description of an image is separated from the medical image itself. This is done to protect the privacy. However, such separation causes problems as well. First one is an increase in the storage space. Second, the two separated storage spaces shall be linked somehow, and this leads to an overhead.

We aim to resolve these problems using the steganography method. Steganography can be used

---

[3] [Online]. Available: https://www.git-scm.com/

to hide the patient private information within a medical image itself. Namely, the private information part and the image do not need to be separated using this method. As a result, applying steganography to medical images allows reducing medical record fragmentation: the personal information of patients is stored together with the medical image itself.

Furthermore, we encrypt sensitive medical images before uploading them into the global IPFS network to prevent unauthorized access. Participants can view sensitive medical images securely by swapping encryption keys. This approach ensures data originality and security, and allows preventing the data from being leaked by unauthorized and irrelevant users and being exposed to malicious attacks, such as eavesdropping, phishing, and brute force attacks [166].

Steganography and encryption methods are discussed in detail below.

Steganography: the least significant bit (LSB)-based steganography technique [167] is used to embed the patient private information, such as name, age, date, diagnostic summary, and physician name into an image without showing the trace of existence of such information. This is performed in such a way that only the sender and recipient are aware of existence of the concealed information.

The resulting image object obtained after embedding the information into the image is called a stego image. The LSB-based encoding method is applied to convert the information into the ASCII code and a binary string. The text is not noticeable, as it is encoded with ASCII and mixed with gray-level bits.

An example of the single-character encoding process is provided below. The similar procedure is applicable to all types of characters:

(1) Convert the patient data into ASCII numbers; each character of the text is converted to its equivalent ASCII number (e.g., "A" = 65).

(2) An ASCII number is converted to an 8-bit binary number.

(3) The binary data are embedded in the original image by sequentially altering the LSB of the image data (LSB of each pixel) by satisfying the following conditions:

✓ If LSB $L(i, j)$ of the original image $O(i, j)$ is equal to any individual binary bit (*IBB*) of the letter "A," then $O(i, j)$ remains unchanged; otherwise, LSB is set to the individual binary bit.

The binary number embedding procedure is given below:

$$S(i, j) = O(i, j) - 1, \ if \ LSB(L(i, j)) = 1 \ and \ IBB = 0$$
$$S(i, j) = O(i, j) + 1, \ if \ LSB(L(i, j)) = 0 \ and \ IBB = 1$$
$$S(i, j) = O(i, j), \ if \ LSB(L(i, j)) = IBB$$

Here, $L(i, j)$ is the LSB of cover image $O(i, j)$, and IBB denotes the individual message bit to be embedded. $S(i, j)$ is the stego image.

Encryption: The stego image is further encrypted using the OpenPGP (Pretty Good Privacy) protocol [168]. OpenPGP is a specific implementation of asymmetric encryption that is used to define standard formats for encrypted messages, signatures, and certificates with the purpose of exchanging public keys. Therefore, a pair of asymmetric keys, a public and private one, is generated. The public key is shared openly without compromising the security, while the private key must be kept private. It is owned by the patient secretly and is used to decrypt the image. The advantage of applying this encryption technique is that using the private key, a digital signature of an image is created to verify its authenticity in the event of a malicious attack.

4.4. Overview of the PCIM system

In the proposed PCIM system, medical images are not stored in the blockchain to avoid scaling

to the unmanageable size and thereby, a resulting blockchain bloat. Therefore, in the present study, we modified the Ethereum blockchain for the proposed POC framework to efficiently manage the identity database and access control across participants. This action allows reducing the fees associated with storing images and managing the related database state. The main purpose of this blockchain is to provide distributed immutable on-chain storage for patient's medical image data within a ledger (database). Figure 16 illustrates the blockchain ledger data structure with a PCIM data field added, as it is designed to store the data that patients want to include in a transaction.

Account nonce
Gas price
Gas limit
Ether
Recipient
PCIM data

Figure 16: Blockchain ledger data structure.

In the proposed scheme, the PCIM data field contents include such information as an image hash value (endpoint of an encrypted medical image), patient addresses, timestamp, encryption public key, image description, and a block hash to form an unchangeable record, as each block is linked with the hash of its previous blocks to connect and verify transactions. Every block is updated in the ledger after transactions are approved and recorded by a patient in the network. A transaction consists of a part corresponding to the ledger content signed and sent by a patient to execute SC by paying ether. Then, transaction validation is performed by the selected and approved consortium. As the blockchain is implemented in the healthcare ecosystem, participants seek to achieve decentralizing the process of medical data management.

The overall architecture of the PCIM system framework is illustrated in Figure 17. As it can be seen, it consists of Ethereum and IPFS networks. The Ethereum network is comprised of PCAC-SC and of a blockchain ledger to manage identity and access control within the network. The

resulting encrypted medical images are stored in the IPFS network.
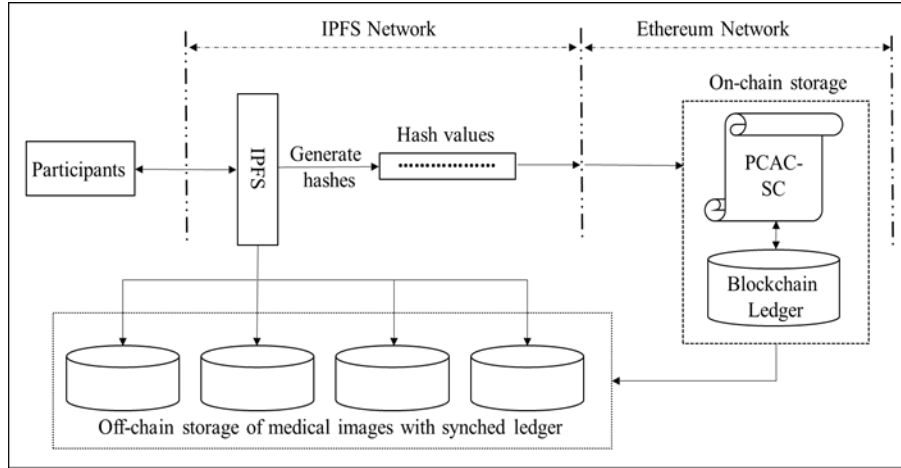
Figure 17: Architecture of patient-centric image management (PCIM) system

4.4.1 System Model

The participants of the proposed PCIM system are defined below:

Patient: Patients are the owners of their medical images. A patient is required to create PCAC-SC and store this SC in the Ethereum blockchain. The patient is responsible for defining the access right to the images in the IPFS network. This definition is done within his/her own PCAC-SC.

Radiologist: A radiologist is able to generate medical images for a patient. The main responsibility of the radiologist is to upload the patient encrypted stego medical images to the IPFS network.

Image Requestors (*IRs*): Doctors, medical institutes, research groups, insurance companies, and general practitioners interested in accessing patient medical images are all considered as image requestors *IRs*. The patient can grant access privileges to any *IRs* based on the authorization policy defined in PCAC-SC.

4.4.2 Ethereum Network: PCAC-SC Protocol

The PCAC-SC protocol uses special functions to provide information about the blockchain and

assign access privileges for *IRs*. The functions of SC are triggered by a patient and *IRs*

entity using their own Ethereum addresses. All triggered functions are stored within the blockchain

ledger as events to allow the entity keeping track of the transaction details. This enables

transparency in the triggered functions and maintains the anonymity of patients by displaying only

events stored in the blockchain. In this framework, we used a single variable and the following

functions:

`msg.sender`: the address variable of the owner who interacts with SC.

`create_contract()`: this function is created and executed only by a patient to issue

corresponding roles for *IRs* and related information for accessing medical images. This function

takes as input a patient's encrypted medical image hash value $h(\overline{I_p})$, blockchain address Φ_P, image

description Δ_P and the timestamp when the function was executed by SC.

`requesting_access()`: this function is executed by *IRs* to obtain access permission from

the patient. *IRs* includes as input the patient blockchain address Φ_P and *IRs* public key K_{IR}^+ to

encrypt medical images and additional information, such as usage notes.

`approve_IRs()`: this function can only be executed by the patient. It grants/denies access

permission by using as input the *IRs* blockchain address Φ_{IR} and notes from *IRs*. The input notes

contain relevant information such as the expiration date and personalization.

`trace_authorization()`: this function is executed by *IRs* and the patient. Authenticity

of digital medical images can be verified by using this authorization function. SC contains the list

of the authorized *IRs* that can access the patient medical image in question.

`remove_IRs()`: this function takes the approved *IRs* blockchain address Φ_{IR} as input and

removes *IRs* from SC upon successful execution of a function by the patient. Consequently, SC is

updated. Therefore, the removed *IRs* has no privilege to access the medical image in question.

Algorithm 1: create_contract()

   Input: $h(\bar{I}_P), \Phi_P , \Delta_P$

   Output: bool

1: **if** *msg.sender* is not Φ_P **then**

2: throw;

3: **end**

4: mapping $h(\bar{I}_P)$ to (Φ_P) and add it to ledger

5: **return** true;

Algorithm 2: requesting_access()

  Input: Φ_P , K^+_{IR}, Notes

  Output: bool

1: **if** *msg.sender* is not Φ_{IR} **then**

2: throw;

3: **end**

4: call PCAC-SC ();

5: **if** new_IRs_address $\Leftarrow$ approved **then**

6: **return** true;

7: **else**

8: **if** new_IRs_address $\Leftarrow$ not approved **then**

9: **return** false;

10: **end**

Algorithm 3: approve_IRs()

   Input: Φ_{IR}, Notes

   Output: bool

1: **if** *msg.sender* is not Φ_P **then**

2: throw;

3: **end**

4: **if** Φ_{IR} exist **then**

5: **return** false;

6: **else**

7: authorize_User[Φ_{IR}] $\Leftarrow$ true;

8: mapping $h(\bar{I}_P)$ to (Φ_{IR}), and add it to ledger

9: **return** true;

10: **end**

Algorithm 4: trace_authorization()

  Input: Φ_P, Φ_{IR}

  Output: bool

1: **if** *msg.sender* is not Φ_{IR} **then**

2: throw;

3: **end**

4: **if** Φ_{IR} exist **then**

5: **return** true;

6: **else**

7: **return** false;

8: **end**

Algorithm 5: remove_IRs

  Input: Φ_{IR}

  Output: bool

1: **if** *msg.sender* is not Φ_P **then**

2: throw;

3: **end**

4: **if** Φ_{IR} is not exist **then**

5: **return** false;

6: **else**

7: authorize_User[Φ_{IR}] $\Leftarrow$ false;

8: **return** true;

9: **end**

4.4.3 IPFS Network

IPFS is used to store encrypted medical images that contain the encrypted patient information in an open distributed storage system, in which images can be exchanged using a hash string path. The paths work similarly to the traditional uniform resource locator used in the web. Therefore, all patient images are always accessible through their hash.

The radiologist uploads medical images of the patient to the system and uses a patient public key to encrypt the images: thereafter, only the patient can decrypt them. Medical image contents are signed by Ethereum private keys of the patient and then, are stored in the blockchain. Therefore, other entities can check the authenticity and integrity of the image ownership using the

content hash and digital signature in the blockchain. In IPFS, files can be accessed even if the host node is offline, as they are located in multiple locations for redundancy. Similarly, when uploading and accessing files on IPFS, it is possible to grant access privileges only to certain users by adding the address of a recipient to PCAC-SC. Therefore, we integrated SC with IPFS to enable authentication of *IRs*. Combining IPFS and the blockchain allows building a permanently addressable on-chain and off-chain data storage that can be linked securely to other significant systems or databases in the world, thereby, forming a global healthcare network.

4.4.4. System Interaction

Fig. 3 illustrates the process of how a patient and a radiologist interact between each other in the part of the proposed PCIM system, where medical image storage and sharing are performed. First, the patient undergoes the medical image examination performed by the radiologist. A medical image I_P of the patient is produced. The patient seeks to have it protected and to maintain the ownership of this image. Consequently, to address this issue, the radiologist encrypts the initial medical image and obtains encrypted image $\bar{I}_P$. Thereafter, the radiologist obtains the hash of the encrypted image $h(\bar{I}_P)$ from the IPFS network and provides the patient with $h(\bar{I}_P)$ for the reference purpose. $h(\bar{I}_P)$ is stored in the blockchain, while the encrypted medical image $\bar{I}_P$ is stored in IPFS. Owing to the fact that the image was encrypted, the patient medical image I_P is accessible only to those who have the decryption key and thereby, it is protected from unauthorized access.
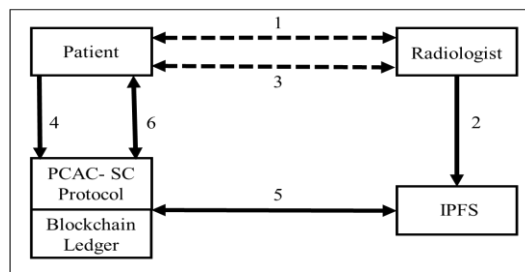
Figure 18: Interaction model of the PCIM system

As presented in Fig.18, the exact protocol for this interaction is explained in detail as follows:

1) Offline interaction between the patient and the radiologist

 a) The patient requests the radiologist to store his/her medical image.

 b) The radiologist asks the patient to provide its encryption key.

c) The patient generates a pair of encryption keys: public K_P^+ and private K_P^- .

d) The patient sends to the radiologist K_P^+ through a secure communication medium.

e) K_P^- is protected and kept safe by the patient.

2) The radiologist encrypts with K_P^+ while concealing the patient private information on a medical

image. Encrypted image $\bar{I}_P$ is uploaded to the IPFS network, which returns a hash $h(\bar{I}_P)$ to the

radiologist.

3) The radiologist shares $h(\bar{I}_P)$ through a secure communication medium with the patient.

4) The patient creates a contract using the PCAC-SC protocol and executes it.

5) The created contract function signs a transaction on the Ethereum blockchain along with

patient public key (Φ_P^+), $h(\bar{I}_P)$, time, image description (Δ_P) such as patient blockchain

address (Φ_P), and an imaging modality from which the data are obtained (e.g., CT, US, MRI,

etc).

6) The patient owns the medical images within the PCIM system. The patient can access, audit,

prove the ownership, and authorize any other *IRs* (e.g., doctors, medical institutes, research groups

and general practitioners) to use their medical images based on PCAC-SC. We discuss the PCAC-

SC interaction sequence in Section V-B.

In summary, a blockchain transaction consists of the following contents signed by a patient to

represent the ownership of the transaction contents:

$$\{\Phi_P, h(\bar{I}_P), \Delta_P\}_{\Phi_P^{-1}}$$

where the part given inside the parenthesis, { }, is the content signed under the Ethereum blockchain private key Φ_P^{-1} of the patient.

4.5 Evaluation

4.5.1 Experiment Setup

A POC design of the PCIM system was developed to test and evaluate its performance. The experiment was conducted using a Windows 10 desktop with an Intel® Core ™ i5-6600 processor at 3.30 GHz. PCAC-SC was implemented in the remix IDE[4] using Solidity[5] programming language. We deployed the program within the private Rinkeby test network using MetaMask[6]. These test network allows obtaining more accurate test results comparing with those to a public blockchain. We initialized IPFS using go-ipfs[7] and uploaded an encrypted stego medical image to the IPFS network from a local computer. This operation returned a unique hash value linked to the uploaded medical image. Thereafter, we updated transactions on the blockchain using create_contract()function by defining the IPFS hash, patient Ethereum public key, and the basic medical image description. Once the block was approved, transactions were stored in the blockchain.

The complete prototype code of PCAC-SC is published in our GitHub repository[8]. The contract deployed on the test network has the following address:

0x5575805E19b4807974Be0B77Fd9d385D4A0e6d1E

---

[4] [Online]. Available: https://remix.ethereum.org/
[5] [Online]. Available: https://solidity.readthedocs.io/en/latest/units-and-global-variables.html
[6] [Online]. Available: https://metamask.io/
[7] [Online]. Available: https://github.com/ipfs/go-ipfs
[8] [Online]. Available: https://github.com/infonetGIST/PCAC-SC

Transactions on each function can be seen using the above address at the Rinkeby Etherscan website[9].

Fig. 19 illustrates such parameters as the block/timeline, functions, and event sequence defined in the PCAC-SC protocol for granting and revoking permissions between a patient and image requestor *IRs* entities. To allow for better understanding of this access sharing sequence, we consider an example of two *IRs*: a doctor (IR_1) and a general practitioner (IR_2) who is interested in accessing a patient medical image.

The patient executes `create_contract()` function by signing the blockchain contents (see Section IV-D). This function allows IR_1 and IR_2 to participate by calling the request function in the PCAC-SC protocol defined by the patient. Each of the entities has its own Ethereum address to perform the operations.

In Figure 19, blocks from 2 to 7 illustrate the access privilege scenario. IR_1 and IR_2 send a request to access medical images using `request_access()` function that is represented by block 2 and block 3. Block 4 and block 5 show that the patient is able to grant and deny the access by using the `approve_IRs()` function. The patient and IR_1 are able to prove the ownership and access privileges by calling `trace_authorization()` function. In Fig.4, block 7 illustrates revoking the permission of IR_1 by calling `remove_IRs()` function, which can be executed only by the patient. The details on execution of each function are stored in the blockchain as an event to help the participants to keep track of their transaction details.

---

[9] [Online]. Available: https://rinkeby.etherscan.io/
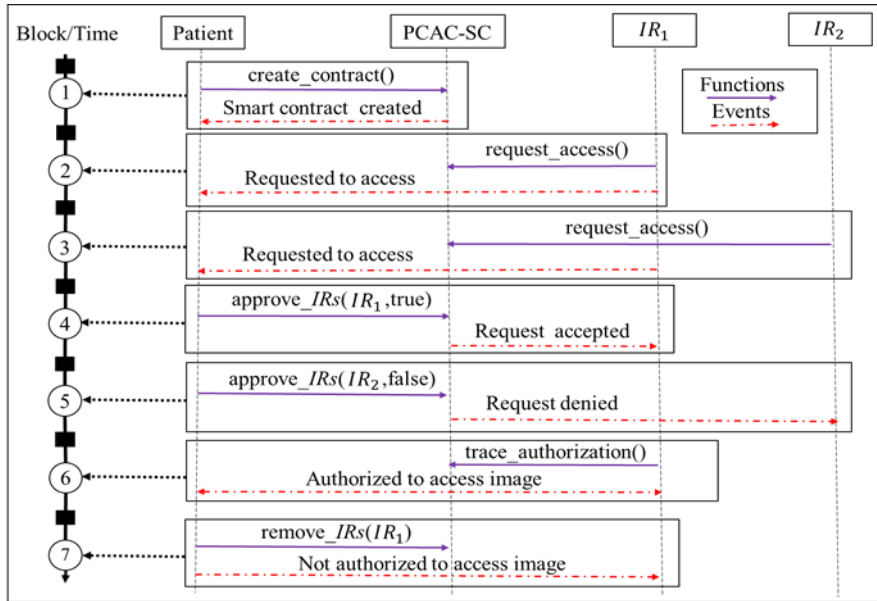
Figure 19: Access sharing sequence. The blockchain/timeline is shown on the left, pointing with dotted arrows for reference. The purple, and red arrows represent interactions between entities.

4.5.2 PCAC-SC Verification

We verify the access sequence and interaction between entities by testing two main functions for brevity. We choose `approve_IRs()` for the accept/deny permission to access a medical image and `traceauthorization()` to verify access privileges for a given Ethereum address. Figure 20 shows that the approved *IRs* and trace authorization functions provide the following test cases: request accepted, request denied, authorization success, and authorization failed.
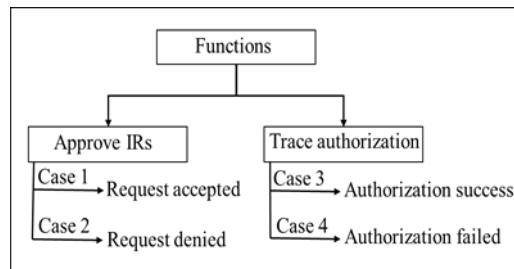
Figure 20: PCAC-SC validating functions and testing cases.

To test the prototype, we consider the following Ethereum address and IPFS hash of the medical image:

Patient Ethereum address:

0x5575805E19b4807974Be0B77Fd9d385D4A0e6d1E

*IR*₁ Ethereum address:

0xdD870fA1b7C4700F2BD7f44238821C26f7392148

*IR*₂ Ethereum address:

0x583031D1113aD414F02576BD6afaBfb302140225

IPFS hash: QmNaS5gQzoPxr3S2n6T6BsFuVRmMFwpohLVFfAFrU8gyTq

Testing an approved IRs function

In this testing, we consider the first case, where a patient approves the *IR*₁ address to access medical images by mapping with the IPFS hash value. Events requestaccepted and approved were triggered by approved_IRs() function, and *IR*₁ gained access privileges to a patient medical image. The event is stored in the blockchain as shown in Figure 21.

```
[
        {
                "from": "0xac9d443f875536ce1346e38550857061c019094b",
                "topic":
"0x8848ffe7bacf0d3c19a311adb625e883f370b9dcbac34384bc6240fa4b1461b4",
                "event": "Requestaccepted",
                "args": {
        "patient":"0x5575805E19b4807974Be0B77Fd9d385D4A0e6d1E",
                        "info": "approved by patient.",
                        "length": 2
                }
        },
        {
                "from": "0xac9d443f875536ce1346e38550857061c019094b",
                "topic":
"0xe3053523a3a35835db28369b20a103b8fe2f7d12c0a6b61b8c23dfe4d5baed65",
                "event": "Approved",
                "args": {
                        "requester":
"0xdD870fA1b7C4700F2BD7f44238821C26f7392148",
                        "info": "Authorized to access image",
                        "length": 2
                }
        }
]
```

Figure 21: Case 1: event log for approving *IR*₁ address to access a patient medical image.

Figure 22 shows the second test case, where a patient denies *IR*₂ request to access medical images. This function triggers two events requestdenied and reason for rejecting by the patient.

```
[
        {
                "from": "0xac9d443f875536ce1346e38550857061c019094b",
        "topic":"0x75fd1545fc54d42c1c105027968847e19149f69adb83be50d44a109a72c2fb1b",
                "event": "Requestdenied",
                "args": {
        "patient":"0x5575805E19b4807974Be0B77Fd9d385D4A0e6d1E",
                        "info": "Failed to be approved by patient",
                        "length": 2
                }
        },
        {
                "from": "0xac9d443f875536ce1346e38550857061c019094b",
        "topic":"0x560ccc9eee914fbea6dc97d101c07c4c563f85a3000c838161a83f8fe0405a43",
                "event": "Reason",
                "args": {
                        "requester": "0x583031D1113aD414F02576BD6afaBfb302140225",
                        "info": " Need more detailed information to access my image",
                        "length": 2
                }
        }
]
```

Figure 22: Case 2: event log stored in the blockchain for denying access to IR_2 address.

Testing trace authorization function

Here, we test the `trace_authorization()` function. This function is used to prove the ownership and trace history of the approved *IR's* in the blockchain. To verify authorization, let us consider that the IR_1 address is already approved. Patient and IR_1 Ethereum address are given as input to execute `trace_authorization()` function, and this triggers authorizationSuccess event. Figure 23 shows the event log of the third test case where IR_1 address is authorized to access an image by the patient.

```
[
        {
                "from": "0xac9d443f875536ce1346e38550857061c019094b",
                "topic":
        "0x59b56ffb470a9c0f006904d6c1037d2eeec29ab337e2690fcdef7e62cf52b1ce",
                "event": "AuthorizationSuccess",
                "args": {
                        "requester":
        "0xdD870fA1b7C4700F2BD7f44238821C26f7392148",
                        "info": "Authorized to access image by:",
                        "patient":
        "0x5575805E19b4807974Be0B77Fd9d385D4A0e6d1E",
                        "length": 3
                }
        }
]
```

Figure 23: Case 3: event log stored in the blockchain. Information shows that the IR_1 address was authorized to access a patient medical image.

Figure 24 shows the log of `authorizationfailed` event invoked from SC. This event occurs due to the fact that the IR_1 address has been removed or has not been approved by the patient.

```
[
        {
                "from": "0xac9d443f875536ce1346e38550857061c019094b",
                "topic":
"0x56d9b42fee56a07a830b34605f693fa0593126978262abc43bcf0f0d62f3b861",
                "event": "AuthorizationFailed",
                "args": {
                        "requester":
"0x583031D1113aD414F02576BD6afaBfb302140225",
                        "info": "Liver image is not authorized to access
by:",
                        "patient":
"0x5575805E19b4807974Be0B77Fd9d385D4A0e6d1E",
                        "length": 3
                }
        }
]
```

Figure 24: Case 4: event log where the address is not authorized to access a patient medical image.

4.5.3 PCIM System Analysis

In the previous sections, we have demonstrated how a medical image can be stored and shared in a decentralized network using the PCIM system. In this section, we analyze the advantages, cost, and feasibility of the proposed framework.

Security and Privacy

Encryption provides a capability of preventing unauthorized users from accessing medical images without private keys. The steganography technique provides users with the ability to verify the originality of an image by extracting the protected patient private information. Furthermore, an IPFS hash value is mapped with the approved *IRs* blockchain address. Therefore, approved users have access privileges and can decrypt medical images using their asymmetric private keys.

Costs and Practicality

In the implemented PCAC-SC prototype, we set a gas limit of 30,000, where each unit of gas is set equal to 2 Gwei. The total transaction fee (gas used $\times$ gas price = ether and USD) in this scenario is 0.11 USD. Table 4 summarizes the cost of the executed operations in SC. The `create_contract()` function is implemented once with a cost of 0.025 USD. The

`request_access()` function cost is 0.093 USD, which is higher than that of other functions due to the additional input bytes included during the function execution, such as those corresponding to the patient blockchain address and notes for the usage agreement. The overall costs can be decreased further if the size of the input data is minimal.

However, these costs are still lower than those associated with buying a storage space from a third-party service or maintaining a database using a centralized system.

Table 4: PCAC-SC cost analysis (gasprice = 2 Gwei,1 ether = 187 USD)

Function	Gas Used	Actual Cost(ether)	USD
create_contract()	67394	0.000134788	0.025
requesting_access()	246908	0.000493816	0.093
approve_IRs()	170412	0.000340824	0.064
trace_authorization()	34266	0.000068532	0.013
remove_IRs()	59358	0.000118716	0.022

Efficient storage of medical images

The use of IPFS allows constructing a high-throughput content-based storage model with content-addressed hyperlinks. The benefits of this storage model include the following ones:

a) Content addressing: medical images have a unique identifier (cryptographic hash of an image).

b) Original content: medical images with the same content cannot be duplicated and are stored only once.

c) Tamper proof: an image is verified based on its checksum; if the hash changes, IPFS recognizes that an image was tampered with.

d) Archiving: offline data access and immutable data storage are useful to get immediate local access to medical images even in the cases with a weak healthcare infrastructure.

e) Reduced data scattering: the patient private information is encrypted in medical images themselves. Therefore, the data are stored in a single node occupying less volume and reducing the burden of data management.

Interoperability

Blockchain technology cryptographically protects the state of transactions of medical images. It also protects transaction integrity using a digital signature. Image file management is transparent, and network peers can verify authenticity of the image ownership.

Full Control Over Medical Images

A patient owns a medical image and can monitor it online. Patients have the complete transparency over their medical images and can provide permission to access or revoke an image from being used in clinical trials or for research purposes. Consequently, the frauds related to health records can be limited. PCAC-SC provides the patients with complete flexibility to add or revoke *IRs* within the system.

Prevent Fraudulent Claims

Let us suppose a case when a patient discovers that his or her decrypted image has been misused by a requester who was already granted with access to medical images. A patient can then immediately claim the ownership of the image. This is performed by the blockchain signature tool[10] that compares a signature hash and the original image contents that were signed by patient. Therefore, fraudulent claims can be prevented in various applications, such as insurance and unauthorized monetization of medical images.

---

[10] [Online]. Available: https://etherscan.io/verifySig

Table 5: Compare between the existing and proposed PCIM system

Schemes	ISN [153]	MedBlock [161]	MeDShare [5]	MedChain [162]	PCIM system
Source data storage	PACS	Dedicated servers	Cloud server	Mutable P2P Storage	Immutable IPFS Storage
Source data encryption / Scheme	Yes / Not mentioned	Yes / Symmetric encryption	Yes / Not mentioned	Yes / Asymmetric encryption	Yes / Asymmetric encryption
Type of data	Medical Images	EMR	EMR	EHR	Medical images + Health records
Server attack resistance	No	No	No	No	Yes
Tamper-proof database	No	Yes	Yes	Yes	Yes
Database sharing mechanism	PACS	Blockchain	Blockchain	Blockchain	Blockchain
Database management	Centralized	Centralized	Centralized	Semi-centralized	Decentralized
Offline data access	No	No	No	No	Yes

Comparison with Existing and Proposed Framework

Table 5 provides the comparison between the proposed framework using an ISN [153] and alternative blockchain-based medical health record management frameworks [24–26]. From this table, it can be seen that the proposed PCIM system has greater advantages comparing with the existing alternatives. Among them, studies [5], [153], [161] are based on centralized frameworks in which one central node failure causes a fail of the whole system. In contrast, in the framework proposed in this paper, every node is independent of each other, which ensures robust and efficient data access. The MedChain [162] uses a mutable P2P storage network, which has a high risk of data attacks and content duplication. The proposed PCIM system overcomes these disadvantages by using an IPFS-based storage in which medical images corresponding to the same content are not allowed being duplicated. This allows users to have full control of their medical images by ensuring guaranteed security, transparency, and data integrity. However, if the contents in a file stored within the IPFS network are not peered or active for a period of time, it is recycled by the garbage collector. Therefore, at least one peer within the network needs to monitor user files and user interest in storing the content.

4.6 Discussion

In this chapter, we presented the POC design of the proposed PCIM system: An Ethereum blockchain and IPFS-based decentralized framework for storing and sharing medical images. Moreover, we introduced a new access management system called PCAC-SC that enables authorized entities to access the relevant blockchain data. The PCIM system facilitates a new way to improve the right of patients to perform self-determination regarding their medical images. The proposed architecture allows protecting the basic health record information of patients including medical images and guarantees privacy by using the combination of steganography and encryption. Moreover, the proposed approach allows reducing fragmentation of the medical health records and ensuring that only authorized persons can get access to the original medical images within an open network. We performed the experimental implementation to analyze and evaluate rationality and feasibility of the proposed scheme. The proposed system facilitates patient access to an immutable medical database providing higher efficiency, data provenance, and effective audit while sharing medical images. The data storage and exchange model is also decentralized; therefore, necessity to involve third-party intermediaries and administrative structures is eliminated.

Chapter 5

Summary

5.1 Thesis summary

The aim of this thesis were focused on improving medical image analysis, reconstruction, and management using advanced technologies. The summary of contributions is as follows:

- ➢ We investigated the methods for early detection of liver cancer using a computer-aided diagnostic system.

- ➢ We proposed a multiplicative speckle suppression technique for ultrasound liver images, based on a new signal reconstruction model known as sparse representation over dictionary learning.

- ➢ We presented the POC design of the proposed PCIM system: An Ethereum blockchain and IPFS-based decentralized framework for storing and sharing medical images.

- ➢ We introduced a new access management system called PCAC-SC that enables authorized entities to access the relevant blockchain data.

5.2 Conclusion and future research directions

This dissertation focuses on solving three distinct issues related to medical imaging techniques: 1) image analysis, 2) image reconstruction, and 3) image management.

The application of the CAD system to imaging informatics demonstrated their importance in image analysis. This study proposed in a new way of categorizing and summarizing the different stages of the computerized system scheme applied to the US liver images with a focus on cancer diagnosis. The systematic review helps to highlight the strengths and weaknesses associated with the choice of the algorithm used for US image analysis.

In particular, data preprocessing is the first and most vital step in the CAD system process because it reconstructs an image without eliminating the important features by reducing signal-dependent multiplicative noise called speckle. Therefore, we presented a multiplicative speckle suppression technique for US liver images, based on a new signal reconstruction model known as sparse representation over dictionary learning. In the proposed technique, the non-uniform multiplicative signal is first converted into additive noise using an enhanced homomorphic filter. This is followed by pixel-based total variation regularization and patch-based SR over a dictionary trained using K-singular value decomposition. Finally, the split Bregman algorithm is used to solve the optimization problem and estimate the de-speckled image. Simulations on both, synthetic and clinical ultrasound images for speckle reduction, have been performed. The proposed technique achieved peak signal-to-noise ratios of 35.537 dB for the dictionary trained on noisy image patches and 35.033 dB for the dictionary trained using a set of reference ultrasound image patches. Further, the evaluation results show that the proposed method performs better than other state-of-the-art denoising algorithms in terms of both peak signal-to-noise ratio and subjective visual quality assessment.

Finally, for a decentralized image management system, we proposed a novel proof-of-concept design for a distributed patient-centric image management system that is aimed to ensure safety and control of patient private data without using any centralized infrastructure. In this system, we

employed an Ethereum blockchain and a distributed file system technology called InterPlanetary file system. Then, we implemented an Ethereum smart contract called the patient-centric access control protocol to enable a distributed and trustworthy access control policy. IPFS provides the means for decentralized storage of medical images with global accessibility. The PCIM system ensures a high level of data security and reduces the fragmentation of patient health records by applying the steganography and asymmetric cryptographic technique.

We described how the PCIM system architecture facilitates the distributed and secured patient-centric data access across multiple entities such as hospitals, patients, and image requestors. Finally, we conducted an experiment to test the framework within the Windows environment and deployed a smart contract prototype on an Ethereum testnet blockchain. The experimental results demonstrated that the proposed scheme is feasible.

However, in the implemented prototype model, medical images are manually uploaded by an image provider into the IPFS network. This process can be enhanced by developing an application programming interface to facilitate a user-friendly access to the system. Furthermore, our future research goal is to deploy the proposed POC design in the public blockchain using real-time scenarios to form a global PCIM system and to validate the proposed approach across a broader set of scenarios.

Our future research will be introducing a novel CAD algorithm for multimodal imaging systems that accurately characterize and detect lesions by including more features and classification techniques such as deep learning, and dictionary learning. Explorations on these new frontiers are likely to bring us more successful applications in medical image processing.

Bibliography

[1]   B. Branstetter, *Basics of Imaging Informatics*. Radiology, 2007.

[2]   I. Bankman, *Handbook of Medical Image Processing and Analysis*. Elsevier, 2009.

[3]   P. Anton, "Medical Image Processing: From Formation to Interpretation," *Analog Devices*.

[4]   M. L. Giger, "Computerized analysis of images in the detection and diagnosis of breast cancer," *Semin. Ultrasound, CT MRI*, vol. 25, no. 5, pp. 411–418, 2004.

[5]   Q. Xia, E. B. Sifah, K. O. Asamoah, J. Gao, X. Du, and M. Guizani, "MeDShare: Trust-Less Medical Data Sharing among Cloud Service Providers via Blockchain," *IEEE Access*, vol. 5, pp. 14757–14767, 2017.

[6]   D. Bartuschat, a Borsdorf, H. Köstler, R. Rubinstein, and M. Stürmer, "A parallel K-SVD implementation for CT image denoising," *Dep. Comput. ...*, vol. 10, pp. 1–26, 2009.

[7]   K. Doi, "Overview on research and development of computer-aided diagnostic schemes," *Semin. Ultrasound, CT MRI*, vol. 25, no. 5, pp. 404–410, 2004.

[8]   H. Yoshida and A. H. Dachman, "Computer-aided diagnosis for CT colonography.," *Semin. Ultrasound. CT. MR*, vol. 25, no. 5, pp. 419–31, Oct. 2004.

[9]   Q. Li *et al.*, "Computer-aided diagnosis in thoracic CT.," *Semin. Ultrasound. CT. MR*, vol. 26, no. 5, pp. 357–63, Oct. 2005.

[10]   J. Y. Wu *et al.*, "Quantitative ultrasound texture analysis for clinical decision making support," vol. 9419, p. 94190W, 2015.

[11]   U. R. Acharya *et al.*, "Decision support system for fatty liver disease using GIST descriptors

extracted from ultrasound images," *Inf. Fusion*, vol. 29, pp. 32–39, 2016.

[12]   J. N. Mait, G. W. Euliss, and R. A. Athale, "Computational imaging," *Adv. Opt. Photonics*, vol. 10, no. 2, pp. 409–483, 2018.

[13]   "Computational imaging." [Online]. Available: https://en.wikipedia.org/wiki/Computational_imaging.

[14]   B. Erickson, "Experience with Importation of Electronic Images into the Medical Record from Physical Media," *J Digit Imaging*, vol. 24, no. 4, pp. 694–699, 2011.

[15]   "DICOM." [Online]. Available: http://en.wikipedia.org/wiki/DICOM. [Accessed: 05-Jan-2019].

[16]   O. Asan, B. Crotty, S. Nagavally, and L. E. Egede, "Patient Centered Communication and E-Health Information Exchange Patterns: Findings From a National Cross-Sectional Survey," *IEEE J. Transl. Eng. Heal. Med.*, vol. 7, pp. 2168–2372, 2018.

[17]   M. Zhang and Ji. Yohong, "Blockchain for healthcare records: a data perspective," *PeerJ Prepr.*, no. May, pp. 2–6, 2018.

[18]   J. D. Halamka, A. Lippman, and A. Ekblaw, "The Potential for Blockchain to Transform Electronic Health Records," *Harvard Business Review,* 2017.

[19]   M. Y. Jabarulla and H. N. Lee, "Computer aided diagnostic system for ultrasound liver images: A systematic review," *Optik (Stuttg).*, vol. 140, pp. 1114–1126, 2017.

[20]   M. Y. Jabarulla and H. N. Lee, "Speckle reduction on ultrasound liver images based on a sparse representation over a learned dictionary," *Appl. Sci.*, vol. 8, no. 6, 2018.

[21]   M. Y. Jabarulla and H. N. Lee, "Evaluating the effect of various speckle reduction filters on

ultrasound liver cancer images," *Int. Conf. Electron. Inf. Commun. ICEIC 2018*, vol. 2018-Janua, pp. 1–4, 2018.

[22] M. Y. Jabarulla and H. N. Lee, "Blockchain-Based Distributed Patient-Centric Image Management System," 2020. arXiv, preprint arXiv:2003.08054.

[23] S. Marwaha, H. Monga, S. M. Student, and H. Cse, "Automatic Diagnosis Systems Using Image Processing- A systematic Study," *IRACST -International J. Comput. Sci. Inf. Technol. Secur.*, vol. 2, no. 2, pp. 2249–9555, 2012.

[24] G. Litjens, O. Debats, J. Barentsz, N. Karssemeijer, and H. Huisman, "Computer-aided detection of prostate cancer in MRI.," *IEEE Trans. Med. Imaging*, vol. 33, no. 5, pp. 1083–92, May 2014.

[25] Gunasundari S, "A Study of Textural Analysis Methods for the Diagnosis of Liver Diseases from Abdominal Computed Tomography," *Int. J. Comput. Appl.*, vol. 74, no. 11, pp. 975–8887, 2013.

[26] D. Jemal, A; Bray, F; Center, MM; Ferlay, J; Ward, E; Forman, "Global cancer statistics," *A cancer J. Clin.*, vol. 61, no. 2, pp. 69–90, 2011.

[27] H. Yoshida, D. D. Casalino, B. Keserci, A. Coskun, O. Ozturk, and A. Savranlar, "Wavelet-packet-based texture analysis for differentiation between benign and malignant liver tumours in ultrasound images.," *Phys. Med. Biol.*, vol. 48, no. 22, pp. 3735–53, Nov. 2003.

[28] G. Xian, "An identification method of malignant and benign liver tumors from ultrasonography based on GLCM texture features and fuzzy SVM," *Expert Syst. Appl.*, vol. 37, no. 10, pp. 6737–6741, 2010.

[29] R. S. C. Cobbold, *Foundations of Biomedical Ultrasound*. Oxford University Press, 2007.

[30] S. Tang and S.-P. Chen, "An Effective Data Preprocessing Mechanism of Ultrasound Image Recognition," *Bioinforma. Biomed. Eng. 2008. ICBBE 2008. 2nd Int. Conf.*, pp. 2708–2711, 2008.

[31] Sk. Narayanan, "A View on Despeckling in Ultrasound Imaging," *Int. J. Signal Process. Image Process. Pattern Recognit.*, vol. 2, no. 3, 2009.

[32] J.-S. Lee, "Digital Image Enhancement and Noise Filtering by Use of Local Statistics," *IEEE Trans. Pattern Anal. Mach. Intell.*, vol. PAMI-2, no. 2, pp. 165–168, Mar. 1980.

[33] J.-S. Lee, "Refined filtering of image noise using local statistics," *Comput. Graph. Image Process.*, vol. 15, no. 4, pp. 380–389, 1981.

[34] D. Kuan, A. Sawchuk, T. Strand, and P. Chavel, "Adaptive restoration of images with speckle," *IEEE Trans. Acoust.*, vol. 35, no. 3, pp. 373–383, Mar. 1987.

[35] R. C. Gonzalez and R. E. Woods, "Digital Image Processing," *Addison-Wesley Publ. Co.*, 2002.

[36] W. N. M. and P. L. A. T. Loupas, "An Adaptive Weighted Median Filter for Speckle Suppression in Medical Ultrasound Images," *IEEE Trans. Circuits Syst.*, vol. Vol. 36., no. January, pp. 129-135., 1989.

[37] R. C. G. and R.E.Woods, "Digital Image Processing," *3rd ed. Pearson Educ.*, 2008.

[38] A. K. Jain, *Fundamentals of digital image processing*. Prentice-Hall, Inc., 1989.

[39] A. Lopes, R. Touzi, and E. Nezry, "Adaptive Speckle Filters and Scene Heterogeneity," *IEEE Trans. Geosci. Remote Sens.*, vol. 28, no. 6, pp. 992–1000, 1990.

[40]   A. Lopes, E. Nezry, R. Touzi, and H. Laur, "Maximum A Posteriori Speckle Filtering And First Order Texture Models In Sar Images," *10th Annu. Int. Symp. Geosci. Remote Sens.*, pp. 8–11, 1990.

[41]   V. S. Frost, J. A. Stiles, K. S. Shanmugan, and J. C. Holtzman, "A model for radar images and its application to adaptive digital filtering of multiplicative noise.," *IEEE Trans. Pattern Anal. Mach. Intell.*, vol. 4, no. 2, pp. 157–66, Feb. 1982.

[42]   D. T. Kuan, a a Sawchuk, T. C. Strand, and P. Chavel, "Adaptive noise smoothing filter for images with signal-dependent noise.," *IEEE Trans. Pattern Anal. Mach. Intell.*, vol. 7, no. 2, pp. 165–177, 1985.

[43]   P. Perona and J. Malik, "Scale-space and edge detection using anisotropic diffusion," *IEEE Trans. Pattern Anal. Mach. Intell.*, vol. 12, no. 7, pp. 629–639, Jul. 1990.

[44]   R. de Luis-García, R. Deriche, M. Rousson, and C. Alberola-López, "Tensor Processing for Texture and Colour Segmentation," 2005, pp. 1117–1127.

[45]   T. D, "Anisotropic diffusion PDE's for image regularization and visualization," *Handb. Math. Methods Imaging, 1st Ed.*, 2010.

[46]   C. Tomasi and R. Manduchi, "Bilateral Filtering for Gray and Color Images," *Int. Conf. Comput. Vis.*, pp. 839–846, 1998.

[47]   S. T. Acton, "Deconvolutional speckle reducing anisotropic diffusion," *Proc. - Int. Conf. Image Process. ICIP*, vol. 1, no. 11, pp. 5–8, 2005.

[48]   S. Mallat, "A Wavelet Tour of Signal Processing," *2nd ed. Acad. Press*, 1999.

[49]   X. Q. Gao, T. Q. Nguyen, and G. Strang, "A study of two-channel complex-valued

filterbanks and wavelets with orthogonality and symmetry properties," *IEEE Trans. Signal Process.*, vol. 50, no. 4, pp. 824–833, 2002.

[50] J. NEUMANN and G. STEIDL, "Dual-Tree Complex Wavelet Transform in the Frequency Domain and an Applicatons to Signal Classification" *Int. J. Wavelets, Multiresolution Inf. Process.*, vol. 03, no. 01, pp. 43–65, Mar. 2005.

[51] N. Kingsbury, "Complex Wavelets for Shift Invariant Analysis and Filtering of Signals," *Appl. Comput. Harmon. Anal.*, vol. 10, pp. 234–253, 2001.

[52] N. Kingsbury, "Image processing with complex wavelets," *Philos. Trans. R. Soc. A Math. Phys. Eng. Sci.*, vol. 357, no. 1760, pp. 2543–2560, Sep. 1999.

[53] M. N. Do and M. Vetterli, "Contourlets: a directional multiresolution image representation," in *Proceedings. International Conference on Image Processing*, 2002, vol. 1, pp. I-357-I–360.

[54] Emmanuel J. Cand`es and David L. Donoho, *Curvelets – A Surprisingly Effective Nonadaptive Representation For Objects with Edges*, Saint-Malo. Vanderbilt University Press, 2000.

[55] A. M. Eskicioglu and P. S. Fisher, "Image quality measures and their performance," *IEEE Trans. Commun.*, vol. 43, no. 12, pp. 2959–2965, 1995.

[56] E. J. Can and D. L. Donoho, "Ridgelets: a key to higher-dimensional intermittency?," *Phil. Trans. R. Soc. Lond.A*, vol. 14, pp. 423–438, 1999.

[57] E. J. Candès and D. L. Donoho, "New tight frames of curvelets and optimal representations of objects with piecewise C^2 singularities," *Commun. Pure Appl. Math.*, vol. 57, no. 2, pp.

219–266, Feb. 2004.

[58]   K. D. Toennies, "Guide to Medical Image Analysis Methods and Algorithms," *Adv. Comput. Vis. Pattern Recognit.*, no. 2191–6586, pp. 1–19, 2012.

[59]   T.Sheela and M.S.Abirami, "Analysis of Image Segmentation Techniques for Medical Images," in *Proceedings of International Conference on Emerging Research in Computing, Information, Communication and Applications*, 2014.

[60]   E. P. Thakur and E. N. Madaan, "A survey of image segmentation techniques," *Int. J. Res. Comput. Appl. Robot. www.ijrcar.com*, vol. 24, pp. 158–165, 2014.

[61]   M.Suganthi and P.Elayaraja, "A survey of image segmentaion techniques," *Int. J. Adv. Res. Comput. Commun. Eng.*, vol. 3, no. 11, 2014.

[62]   R. Adams and L. Bischof, "Seeded region growing," *IEEE Trans. Pattern Anal. Mach. Intell.*, vol. 16, no. 6, pp. 641–647, Jun. 1994.

[63]   R. M. S. and K. S. Selvanayaki, "A Survey on Image Segmentation Techniques for Edge Detection," in *International Conference on Innovation in Communication, Information and Computing (ICICIC)*, 2013.

[64]   A. A. M. Rajiv Kumar, "A Comparative Study of Image Segmentation Using Edge-Based Approach," *Int. J. Math. Comput.*, vol. 7, no. 3, 2013.

[65]   S. Saleh Al-Amri, N. V Kalyankar, and K. S. D, "Image Segmentation by Using Threshold Techniques," *J. Comput.*, vol. 2, no. 5, pp. 2151–9617, 2010.

[66]   V. D. Santanu Bhowmik, "A Survey on Clustering Based Image Segmentation," *Int. J. Adv. Res. Comput. Eng. Technol.*, vol. 1, no. 5, pp. 2278–1323, 2012.

[67] O. Oke, T. Adedeji, O. Alade, and E. Adewusi, "Fuzzy kc-means Clustering Algorithm for Medical Image Segmentation," *J. Inf.*, vol. 2, no. 6, pp. 21–33, 2012.

[68] R. R. and K. Tejaswini, "A Survey of Image Segmentation Algorithms Based On Fuzzy Clustering," *Int. J. Comput. Sci. Mob. Comput.*, vol. 2, no. July, pp. 200–206, 2013.

[69] I. Levner, V. Bulitko, and G. Lin, "Feature Extraction for Classification of Proteomic Mass Spectra: A Comparative Study," in *Feature Extraction*, Berlin, Heidelberg: Springer Berlin Heidelberg, pp. 607–624.

[70] K. I. Laws, "Texture energy measures," in *Image understanding workshop*, 1979, pp. 47–51.

[71] R. M. Haralick, K. Shanmugam, and I. Dinstein, "Textural Features for Image Classification," *IEEE Trans. Syst. Man. Cybern.*, vol. 3, no. 6, pp. 610–621, Nov. 1973.

[72] M.M.Galloway, "Texture classification using gray level run lengths," *Comput. Graph. Image Process.*, vol. 4, pp. 172–179, 1975.

[73] D. Gaitini *et al.*, "Feasibility study of ultrasonic fatty liver biopsy: Texture vs. attenuation and backscatter," *Ultrasound Med. Biol.*, vol. 30, no. 10, pp. 1321–1327, Oct. 2004.

[74] W.-C. Yeh, S.-W. Huang, and P.-C. Li, "Liver fibrosis grade classification with B-mode ultrasound.," *Ultrasound Med. Biol.*, vol. 29, no. 9, pp. 1229–35, Sep. 2003.

[75] Z. Jiang *et al.*, "Support Vector Machine-Based Feature Selection for Classification of Liver Fibrosis Grade in Chronic Hepatitis C," *J Med Syst*, vol. 30, pp. 389–394, 2006.

[76] M. S. Gebbinck, J. T. Verhoeven, J. M. Thijssen, and T. E. Schouten, "Application of neural networks for the classification of diffuse liver disease by quantitative echography.,"

Ultrason. Imaging, vol. 15, no. 3, pp. 205–17, Jul. 1993.

[77] N. H. K.Ogawa,k. Kubota, "Computer-aided Diagnostic System for Diffuse Liver Diseases with Ultrasonography by Neural Networks," *IEEE Trans. Nucl. Sci.*, vol. 45, no. 6, pp. 3069–3074, 1998.

[78] D. Mittal, V. Kumar, S. C. Saxena, N. Khandelwal, and N. Kalra, "Neural network based focal liver lesion diagnosis using ultrasound images," *Comput. Med. Imaging Graph.*, vol. 35, no. 4, pp. 315–323, 2011.

[79] S. Pavlopoulos, E. Kyriacou, D. Koutsouris, K. Blekas, A. Stafylopatis, and P. Zoumpoulis, "Fuzzy neural network-based texture analysis of ultrasonic images," *IEEE Eng. Med. Biol. Mag.*, vol. 19, no. 1, pp. 39–47, 2000.

[80] S.-T. J. Christianini N, "An Introduction to Support Vector Machines and Other Kernel-Based Learning Methods," *United Kingdom: Cambridge University Press*, 2000.

[81] Y. Hirose, K. Yamashita, and S. Hijiya, "Back-propagation algorithm which varies the number of hidden units," *Neural Networks*, vol. 4, no. 1, pp. 61–66, 1991.

[82] G. E. H. and R. J. W. David E.Eumelhart, "Learning representation by back-propagation errors," *Lett. to Nat.*, vol. 323, pp. 533–536, 1986.

[83] P.D.Wasserman, *Advanced Methods in Neural Computing*. Van Nostrand Reinhold, 1993.

[84] F. van der Heijden, R. P. W. Duin, D. de Ridder, and D. M. J. Tax, *Classification, Parameter Estimation and State Estimation: An Engineering Approach Using MATLAB*. Chichester, UK: John Wiley & Sons, Ltd, 2004.

[85] Y. M. Kadah, A. A. Farag, J. M. Zurada, A. M. Badawi, and A. B. M. Youssef,

"Classification algorithms for quantitative tissue characterization of diffuse liver disease from ultrasound images," *IEEE Trans. Med. Imaging*, vol. 15, no. 4, pp. 466–478, 1996.

[86] Y. I. Liu, A. Kamaya, T. S. Desser, and D. L. Rubin, "A Bayesian classifier for differentiating benign versus malignant thyroid nodules using sonographic features.," in *AMIA symposium proceeding*, 2008, pp. 419–23.

[87] H. B. P. P.C.Bhat, "Bayesian Neural Networks," in *Proceedings of PHYSTAT 05*, 2006, pp. 151–155.

[88] W. Zhu, N. Zeng, and N. Wang, "Sensitivity , Specificity , Accuracy , Associated Confidence Interval and ROC Analysis with Practical SAS ® Implementations K & L consulting services , Inc , Fort Washington , PA Octagon Research Solutions , Wayne," *NESUG Heal. Care Life Sci.*, pp. 1–9, 2010.

[89] J. R. Beck and E. K. Shultz, "The use of relative operating characteristic (ROC) curves in test performance evaluation.," *Arch. Pathol. Lab. Med.*, vol. 110, no. 1, pp. 13–20, Jan. 1986.

[90] G. Zhou, Y. Wang, W. Wang, Y. Sun, and Y. Chen, "Decision of Cirrhosis Using Liver's Ultrasonic Images.," in *Proceedings of the 2005 IEEE Engineering in Medicine and Biology*, 2005, vol. 4, pp. 3351–4.

[91] G. Cao, P. Shi, and B. Hu, "Liver fibrosis identification based on ultrasound images.," in *Annual International Conference of the IEEE Engineering in Medicine and Biology Society.*, 2005, vol. 6, pp. 6317–20.

[92] A. Ahmadian, A. Mostafa, M. Abolhassani, and Y. Salimpour, "A texture classification method for diffused liver diseases using Gabor wavelets.," in *IEEE Engineering in Medicine*

and Biology Society., 2005, vol. 2, pp. 1567–70.

[93] D. Balasubramanian, P. Srinivasan, and R. Gurupatham, "Automatic classification of focal lesions in ultrasound liver images using principal component analysis and neural networks.," in *IEEE Engineering in Medicine and Biology Society.*, 2007, pp. 2134–7.

[94] S. Poonguzhali, B. Deepalakshmi, and G. Ravindran, "Optimal Feature Selection and Automatic Classification of Abnormal Masses in Ultrasound Liver Images," in *2007 International Conference on Signal Processing, Communications and Networking*, 2007, pp. 503–506.

[95] J. H. Jeon, J. Y. Choi, S. Lee, and Y. M. Ro, "Multiple ROI selection based focal liver lesion classification in ultrasound images," *Expert Syst. Appl.*, vol. 40, no. 2, pp. 450–457, 2013.

[96] R. Ribeiro, R. Marinho, J. Velosa, F. Ramalho, and J. M. Sanches, "Chronic liver disease staging classification based on ultrasound, clinical and laboratorial data," in *2011 IEEE International Symposium on Biomedical Imaging: From Nano to Macro*, 2011, pp. 707–710.

[97] R. Ribeiro, R. T. Marinho, J. Velosa, F. Ramalho, J. M. Sanches, and J. S. Suri, "The usefulness of ultrasound in the classification of chronic liver disease.," in *IEEE Engineering in Medicine and Biology Society*, pp. 5132–5, 2011.

[98] F. U. A. A. Minhas, D. Sabih, and M. Hussain, "Automated classification of liver disorders using ultrasound images," *J. Med. Syst.*, vol. 36, no. 5, pp. 3163–3172, 2012.

[99] J. S. S. U. Rajendra Acharya, S. Vinitha Sree, Ricardo Ribeiro, Ganapathy Krishnamurthi, Rui Tato Marinho, João Sanches, "Data mining framework for fatty liver disease

classification in ultrasound: A hybrid feature extraction paradigm," *Med. Phys.*, vol. 39, 2012.

[100] J. Virmani, V. Kumar, N. Kalra, and N. Khandelwal, "SVM-based characterization of liver ultrasound images using wavelet packet texture descriptors," *J. Digit. Imaging*, vol. 26, no. 3, pp. 530–543, 2012.

[101] C. Computing, "Prediction of liver cirrhosis based on multiresolution texture descriptors from B-mode ultrasound Jitendra Virmani * and Vinod Kumar Naveen Kalra and Niranjan Khandelwal," vol. X, no. xxxx, pp. 1–19, 2013.

[102] J. Virmani, V. Kumar, N. Kalra, and N. Khandelwal, "A comparative study of computer-aided classification systems for focal hepatic lesions from B-mode ultrasound.," *J. Med. Eng. Technol.*, vol. 37, no. 4, pp. 292–306, May 2013.

[103] N. K. Jitendra Virmani, Vinod Kumar, Naveen Kalra, "PCA -SVM based CA D System for Focal Liver Lesions using B-Mode Ultrasound Images," *Def. Sci. J.*, vol. 63, pp. 478–486, 2013.

[104] M. Roy, "Classification of Ultrasonography Images of Human Fatty and Normal Livers using GLCM Textural Features," vol. 4, no. July, 2014.

[105] V. J., K. V., K. N., and K. N., "Neural network ensemble based CAD system for focal liver lesions from B-mode ultrasound," *J. Digit. Imaging*, vol. 27, no. 4, pp. 520–537, 2014.

[106] V. Morocho, P. Vanegas, and R. Medina, "Hepatic Steatosis Detection Using the Co-occurrence Matrix in Tomography and Ultrasound Images," 2015.

[107] Y. N. Hwang, J. H. Lee, G. Y. Kim, Y. Y. Jiang, and S. M. Kim, "Classification of focal

liver lesions on ultrasound images by extracting hybrid textural features and using an artificial neural network," *Biomed. Mater. Eng.*, vol. 26, no. s1, pp. S1599–S1611, 2015.

[108] C. B. Burckhart, "Speckle in ultrasound B-mode scans," *IEEE Trans Sonics Ultrason*, vol. 30, no. 156–163, 1983.

[109] J. S. Goldstein, I. S. Reed, and L. L. Scharf, "A multistage representation of the Wiener filter based on orthogonal projections," *IEEE Trans. Inf. Theory,* vol. 44, no. 7, pp. 2943–2959, 1998.

[110] P. Simon and H. Patrick, "Median Filtering in Constant Time," *EE Trans. Image Process.*, vol. 16, no. 9, pp. 2389–2394, 2007.

[111] A. Achim, A. Bezerianos, and P. Tsakalides, "Novel Bayesian multiscale method for speckle removal in medical ultrasound images," *IEEE Trans. Med. Imaging*, vol. 20, no. 8, pp. 772–783, 2001.

[112] Z. J. and C. H. Y. Chen, "Efficient Statistical Modeling of Wavelet Coefficients For Image Denoising," *Int. J. Wavelets Multiresolut Inf. Process*, vol. 07, no. 05, 2009.

[113] A. Vishwa and S. Sharma, "Modified Method for Denoising the Ultrasound Images by Wavelet Thresholding," *Int. J. Intell. Syst. Appl.*, vol. 4, no. 6, p. 25, 2012.

[114] Y. Shen, Q. Liu, S. Lou, and Y. L. Hou, "Wavelet-Based Total Variation and Nonlocal Similarity Model for Image Denoising," *IEEE Signal Process. Lett.*, vol. 24, no. 6, pp. 877–881, 2017.

[115] and M. E. A. M. Bruckstein, D. L. Donoho, "From sparse solutions of systems of equations to sparse modeling of signals and images," *SIAM Rev.*, vol. 51, no. 1, pp. 34–81, 2009.

[116] S. Li, G. Wang, and X. Zhao, "Multiplicative noise removal via adaptive learned dictionaries and TV regularization," *Digit. Signal Process.*, vol. 50, pp. 218–228, 2016.

[117] K. Liu, J. Tan, and B. Su, "An Adaptive Image Denoising Model Based on Tikhonov and TV Regularizations," vol. 2014, 2014.

[118] M. Aharon, M. Elad, and A. M. Bruckstein, "The {K-SVD}: An Algorithm for Designing of Overcomplete Dictionaries for Sparse Representations," *IEEE Trans. Signal Process.*, vol. 54, no. 11, pp. 4311–4322, 2006.

[119] P. C. Tay, C. D. Garson, S. T. Acton, and J. A. Hossack, "Ultrasound despeckling for contrast enhancement," *IEEE Trans. Image Process.*, vol. 19, no. 7, pp. 1847–1860, 2010.

[120] T. Joel and R. Sivakumar, "An extensive review on Despeckling of medical ultrasound images using various transformation techniques," *Appl. Acoust.*, vol. 138, no. February, pp. 18–27, 2018.

[121] Y. Youngjian and S. T. Acton, "Speckle reducing anisotropic diffusion," *IEEE Trans. Image Process.*, vol. 11, no. 11, pp. 1260–1270, 2002.

[122] S. A. Hussain and S. M. Gorashi, "Image Denoising based on Spatial/Wavelet Filter using Hybrid Thresholding Function," *Int. J. Comput. Appl.*, vol. 42, no. 13, pp. 0975–8887, 2012.

[123] A. Chambolle, "An algorithm for total variation minimizations and applications," *J. Math. Imaging Vis.*, vol. 10, no. 1–2, pp. 89–97, 2004.

[124] Gilles Aubert and Jean-François Aujol, "A Variational Approach to Removing Multiplicative Noise," *SIAM J. Appl. Math.*, vol. 68, no. 4, pp. 925–946, 2008.

[125] A. Buades, B. Coll, and J. M. Morel, "A Review of Image Denoising Algorithms, with a

New One," *Multiscale Model. Simul.*, vol. 4, no. 2, pp. 490–530, 2005.

[126] S. O. G. Gilboa, "Nonlocal operators with applications to image processing," *SIAM J. Multiscale Model. Simul.*, vol. 7, no. 3, pp. 1005–1028, 2008.

[127] M. Elad and M. Aharon, "Image denoising via sparse and redundant representations over learned dictionaries in wavelet domain," *IEEE Trans. Image Process.*, vol. 15, no. 12, pp. 754–758, 2006.

[128] J. Wright, Y. Ma, J. Mairal, G. Sapiro, T. S. Huang, and S. Yan, "Sparse representation for computer vision and pattern recognition," *Proc. IEEE*, vol. 98, no. 6, pp. 1031–1044, 2010.

[129] T. T. Cai and L. Wang, "Orthogonal matching pursuit for sparse signal recovery with noise," *IEEE Trans. Inf. Theory*, vol. 57, no. 7, pp. 4680–4688, 2011.

[130] B. Deka ; P. K. Bora, "Despeckling of medical ultrasound images using sparse representation," in *International Conference on Signal Processing and Communications (SPCOM)*, 2010, pp. 2165–0608.

[131] R. S. C. Cobbold, *Foundations of Biomedical Ultrasound*. Oxford University Press, 2007.

[132] N. Yahya, N. S. Kamel, and A. S. Malik, "Subspace-based technique for speckle noise reduction in ultrasound images," *Biomed. Eng. Online*, vol. 13, no. 1, p. 154, 2014.

[133] H. H. Arsenault and M. Levesque, "Combined homomorphic and local-statistics processing for restoration of images degraded by signal-dependent noise," *Appl. Opt.*, vol. 23, no. 6, pp. 845–850, 1984.

[134] H. Xie, L. E. Pierce, and F. T. Ulaby, "Statistical properties of logarithmically transformed speckle," *IEEE Trans. Geosci. Remote Sens.*, vol. 40, no. 3, pp. 721–727, 2002.

[135] E. Candes, E. Candes, J. Romberg, and J. Romberg, "l1-magic : Recovery of Sparse Signals via Convex Programming", pp. 1–19, 2005.

[136] M. V. Afonso, J. M. Bioucas-Dias, and M. A. T. Figueiredo, "An augmented lagrangian approach to the constrained optimization formulation of imaging inverse problems," *IEEE Trans. Image Process.*, vol. 20, no. 3, pp. 681–695, 2011.

[137] G. Davis, S. G. Mallat, and M. Avellaneda, "Adaptive Greedy Approximations," *Constr. Approx.*, vol. 13, no. 1, pp. 57–98, 1997.

[138] F. Xiang and Z. Wang, "Split Bregman iteration solution for sparse optimization in image restoration," *Optik (Stuttg).*, vol. 125, no. 19, pp. 5635–5640, 2014.

[139] Z. Wang, A. Bovik, H. Sheikh, and E. Simoncelli, "Image quality assessment: from error visibility to structural similarity," *IEEE Trans Image Process*, vol. 4, no. 13, pp. 600–12, 2004.

[140] L. . Shepp and F. . Logan, "The Fourier reconstruction of a head section," *IEEE Trans. Nucl. Sci.*, vol. 21, no. 3, pp. 21–43, 1974.

[141] F. Llach, "Hypercoagulability, renal vein thrombosis, and other thrombotic complications of nephrotic syndrome," *Kidney Int*, vol. 3, no. 28, pp. 429–39, 1985.

[142] T. Heart, O. Ben-Assuli, and I. Shabtai, "A review of PHR, EMR and EHR integration: A more personalized healthcare and public health policy," *Heal. Policy Technol.*, vol. 6, no. 1, pp. 20–25, 2017.

[143] P. F. Edemekong and M. J. Haydel, *Health Insurance Portability and Accountability Act (HIPAA)*. StatPearls Publishing, 2018.

[144] R. Acharya U., S. Subbanna Bhat, S. Kumar, and L. C. Min, "Transmission and storage of medical images with patient information," *Comput. Biol. Med.*, vol. 33, no. 4, pp. 303–310, 2003.

[145] K. Roth, CJ; Lannum, LM; Persons, "A Foundation for Enterprise Imaging: HIMSS-SIIM Collaborative White Paper," *J Digit Imag*, vol. 29, no. 5, p. 5, 2016.

[146] H. Landi, "Healthcare Data Breach Costs Remain Highest at $408 Per Record," *Helathcare informatics*, 2018. .

[147] S. Nakamoto, "Bitcoin: A peer-to-peer electronic cash system," *Tech. Rep.,* 2008. [Online]. Available: https://bitcoin.org/bitcoin.pdf.

[148] G. Wood, "ETHEREUM: A secure decentralised generalised transaction ledger," *Tech. Rep.*, 2014. [Online]. Available: https://gavwood.com/paper.pdf. [Accessed: 02-Jan-2019].

[149] M. Mettler, "Blockchain technology in healthcare: The revolution starts here," in *IEEE 18th International Conference on e-Health Networking, Applications and Services (Healthcom)*, 2016, pp. 1–3.

[150] J. Benet, "IPFS - Content Addressed, Versioned, P2P File System," 2014.

[151] J. V. Zwanenburg, "4 Decentralized Cloud Storage Platforms That Are Shaking Up The Industry," 2018. [Online]. Available: https://www.investinblockchain.com/decentralized-cloud-storage-platforms/. [Accessed: 10-May-2019].

[152] S. G. Shini, T. Thomas, and K. Chithraranjan, "Cloud based medical image exchange-security challenges," *Procedia Eng.*, vol. 38, pp. 3454–3461, 2012.

[153] S. G. Langer *et al.*, "The RSNA Image Sharing Network," *J. Digit. Imaging*, vol. 28, no. 1,

pp. 53–61, 2014.

[154] R. H. Choplin, J. M. Boehme, and C. D. Maynard, "Picture archiving and communication systems: An overview," *Radiographics*, vol. 12, no. 1, pp. 127–129, 1992.

[155] J. Prince and J. Links, *Medical imaging signals and system*. Pearson Education, 2006.

[156] A. S. Khong, I. Currie, and S. Eccles, "Risk management NHS Connecting for Health and the National Programme for Information Technology Learning objectives : • To understand how engagement with clinicians and representatives from the Ethical issues :," pp. 27–32, 2008.

[157] N. Pouloudi, W. Currie, and E. A. Whitley, "Entangled stakeholder roles and perceptions in health information systems: A longitudinal study of the UK NHS N3 Network," *J. Assoc. Inf. Syst.*, vol. 17, no. 2, pp. 107–161, 2016.

[158] G. Pare and M. C. Trudel, "Knowledge barriers to PACS adoption and implementation in hospitals.," *Int. J. Med. Inform.*, vol. 76, no. 1, pp. 22–33, 2007.

[159] P. Duyck *et al.*, "Monitoring the PACS implementation process in a large university hospital – discrepancies between radiologists and physicians," *J. Digit. Imaging*, vol. 23, no. 1, pp. 73–80, 2010.

[160] C. Beek, "McAfee Researchers Find Poor Security Exposes Medical Data to Cybercriminals," 2018. [Online]. Available: https://securingtomorrow.mcafee.com/other-blogs/mcafee-labs/mcafee-researchers-find-poor-security-exposes-medical-data-to-cybercriminals/. [Accessed: 09-May-2019].

[161] K. Fan, S. Wang, Y. Ren, H. Li, and Y. Yang, "system level quality improvement MedBlock:

Efficient and Secure Medical Data Sharing Via Blockchain," pp. 1–11, 2018.

[162] B. Shen, J. Guo, and Y. Yang, "MedChain: Efficient Healthcare Data Sharing via Blockchain," *Appl. Sci.*, vol. 9, no. 6, p. 1207, 2019.

[163] V. Patel, "A framework for secure and decentralized sharing of medical imaging data via blockchain consensus," *Health Informatics J.*, 2018.

[164] V. Buterin, "Ethereum White Paper." [Online]. Available: https://github.com/ethereum/wiki/wiki/White-Paper. [Accessed: 02-Jan-2019].

[165] F. Bourgeois, O. KL, and M. KF, "Patients Treated at Multiple Acute Health Care Facilities Quantifying Information Fragmentation," *Arch Intern Med.*, vol. 170(22), no. 1989–1995, 2010.

[166] M. G. Gouda, A. X. Liu, L. M. Leung, and M. A. Alam, "SPP: An anti-phishing single password protocol," *Comput. Networks*, vol. 51, no. 13, pp. 3715–3726, 2007.

[167] J. Mamta and P. S. Sandhu, "A New Approach for Information Security using an Improved Steganography Technique," *J Inf Process Syst*, vol. 9, no. 3, 2013.

[168] J. Callas, L. Donnerhacke, H. Finney, D. Shaw, and R. Thayer, "OpenPGP Message Format," *IETF Proposed Standard RFC 4880*, 2007.

Acknowledgments

Firstly, I would like to give my sincerest gratitude to my advisor Prof. Heung No-Lee for his patience, guidance, and mentorship throughout my thesis. I appreciate all his contributions of time, ideas, and funding to make my Ph.D. experience productive and stimulating. The joy and enthusiasm he has for his research were contagious and motivational for me. I give special thanks to him for introducing this field of research and helping me become a researcher, and for all his support in making better at it.

I want to say thanks to my colleagues and seniors in the INFONET Lab, Hwanchul Jang, Wonngbi Lee, Younghak Shin, Seungchan Lee, Sangjun Park, M. Asif Raza, Zafar Iqbal, Oliver James, Nitin Rawat, Jusung Kang, Jehyuk Jang, Pavel Ni, Haeong Choi, Jaewon Bang, Hyeonjun Han, Cheolsun Kim, Rohit Thakur, Hyoungsung Kim, Giljun Jang, Kiwon, ChangYun Lee, and Jeong Park for their support during research. I would always remember my fellow lab mates for the fun-time we spent together and for stimulating the research discussions.

For this dissertation, I would like to thank my committee members: Prof. Boreom Lee, Prof. Kyoobin Lee, Prof. Jonghyun Choi, and Prof. Anil Kumar for their time, interest, helpful comments and insightful questions during my oral defence.

I gratefully acknowledge the funding sources that made my Ph.D. work possible. I was funded by the Korean government scholarship for my entire Ph.D. program and my research work was supported by the National Research Foundation of Korea.

My time at GIST was made enjoyable in large part due to the many international friends and groups that became a part of my life. Especially, I would like to thank all my friends from the GIP program, GIST Indians, and the GIST international community who gave me the necessary distractions from my research and made my stay in Korea memorable and happy.

I cannot forget friends who went through hard times together, cheered me on, and celebrated each accomplishment during my stay in GIST: Dr. Inbarasan, Dr. Muthu Kumar, Dr. Nitin, Dr. Raja, Dr. Yogeenth, and Dr. Guru.

It is a pleasure to thank my brother Uzzain Jabbar, my uncle Mohamed Ali, brother-in-law Raffiudeen, brother Balaji Sadagopan, and friend for life Sathish. They believed, supported, and encouraged me to pursue my higher studies from the beginning.

Curriculum Vitae

Name: Mohamed Yaseen Jabarulla

Birth Date: Sep 28, 1989

Birth Place: Chennai, Tamil Nadu, India.

Temporary Address: Gwangju Institute of Science and Technology, Gwangju, South Korea.

Research Interest

1. Medical image processing

2. Machine learning

3. Blockchain

4. Computational imaging

Education

2016.03–2020.08	Ph.D. Electrical Engineering and Computer Science, Gwangju Institute of Science and Technology (GIST), Gwangju, South Korea.
2014.03–2016.08	M.S. Information and Communication Engineering, Gwangju Institute of Science and Technology (GIST), Gwangju, South Korea.
2008.06–2011.04	B.E. Electronic and Communication Engineering, Anna University, Tamil Nadu, India.
2005.08-2008.04	Diploma in Electronic and Communication Engineering, Technical Education, Government of Tamil Nadu, India

Work Experience

2014.03–Present	Researcher, GIST, Gwangju, South Korea.
2013.11–2014.02	Technical Support Engineer, Concentrix Corporation, Tamil Nadu, India
2012.02–2013.10	System Security Specialist, iOPEX Technologies, Tamil Nadu, India.

Achievements and Awards

1. Received the award of Korean Government Scholarship for Ph.D. study at GIST.

2. Received the award of Korean Government Scholarship for M.S. study at GIST.

3. Received research assistant scholarship for outstanding performance in research during Ph.D. program.

4. Received best employee award (2013) at iOPEX Technologies.

Publications

SCI Journals:

1. **Mohamed Yaseen.J,** Heung-No Lee, "Computer Aided Diagnostic System for Ultrasound Liver Images: A Systematic Review", *Optik - International Journal for Light and Electron Optics Optik*., vol. 140, pp. 1114–1126, July 2017.

2. **Mohamed Yaseen.J,** Heung-No Lee**,** "Speckle Reduction on Ultrasound Liver Images Based on Sparse Representation Over Learned Dictionary" *Applied Sciences-MDPI.* Vol. 8, no, 6, pp 903, May. 2018.

3. **Mohamed Yaseen.J,** Heung-No Lee**,** "Blockchain-Based Distributed Patient-Centric Image Management System", *IEEE Journal of Translational Engineering in Health and Medicine.* (**Status:** Under revision, As of May 2020) arXiv, preprint arXiv:2003.08054.

Conferences:

1. **Mohamed Yaseen.J**, Heung-No Lee**,** "Ultrasound Imaging Super Resolution via Compressive Sensing", ICCAT 2015, Rome, Italy.

2. **Mohamed Yaseen.J**, Heung-No Lee," Compressive Sensing Based Secure Storage and Transmission of Ultrasound Images." ICEIC 2017, Phuket, Thailand.

3. **Mohamed Yaseen.J**, Heung-No Lee," Evaluating the Effect of Various Speckle Reduction Filters on Ultrasound Liver Cancer Images". ICEIC 2018, Hawaii, USA.

4. **Mohamed Yaseen.J**, Giljun Jang and Heung-No Lee," "Decentralized Framework for Medical Images Based on Blockchain and Inter Planetary File System". EMBC 2019, Berlin, Germany.

5. Michele Scarlato, Cristian Perra, **Mohamed Yaseen.J**, Giljun Jung, Heung-No Lee, "A Blockchain For The Collision Avoidance And The Recovery of Crashed UAVs". Korean Institute of Electronics Engineers Conference 2019, Jeju, South Korea.